

**The influence of oceanographic processes on contourite features: A  
multidisciplinary study of the northern South China Sea**

Shaoru Yin<sup>a\*</sup>, F. Javier Hernández-Molina<sup>b</sup>, Wenyan Zhang<sup>c</sup>, Jiabiao Li<sup>a\*</sup>,

Liaoliang Wang<sup>d</sup>, Weifeng Ding<sup>a</sup>, Weiwei Ding<sup>a</sup>

<sup>a</sup> Key Laboratory of Submarine Geosciences, State Oceanic Administration, Second Institute of Oceanography, Ministry of Natural Resources, Hangzhou, 310012, China

<sup>b</sup> Department of Earth Sciences, Royal Holloway, University of London, Egham, Surrey TW20 0EX, UK

<sup>c</sup> Institute of Coastal Research, Helmholtz-Zentrum Geesthacht, Geesthacht, 21502, Germany

<sup>d</sup> Guangzhou Marine Geological Survey, Guangzhou 510075, China

**Abstract**

This study examines how multiscale oceanographic processes interact with the seafloor to influence the development of contourite features in northern part of the South China Sea. The multidisciplinary approach used in this study combines physical oceanographic monitoring, numerical simulation, multibeam echosounding, seismic reflection profiling, and sediment core interpretation. The contourites detected and interpreted herein include depositional (drifts and sediment waves), erosional (channels, moats and furrows), and mixed erosional and depositional features (terraces and irregular depressions). This study finds

---

\* Corresponding author.

E-mail address: jbli@sio.org.cn, shaoru2017@outlook.com

that climatic variation influences the intensity of quasi-steady, along-slope regional water circulation which in turn influences the long-term development of primary (10–100 km) contourite depositional systems. Energetic but intermittent oceanographic processes (such as eddies and internal waves) generate smaller secondary features within the contourite depositional systems resulting in a complex, local seafloor morphology. Westward to south-westward migrating mesoscale eddies locally enhance regional water mass circulation and trigger sub-mesoscale flows which can generate (1–10 km) irregular depressions along their paths. Westward-propagating internal solitary waves form sedimentary waves. With the aid of numerical modelling results, a sedimentary model is proposed to explain how oceanographic processes influence sedimentary processes and determine a hierarchy of associated feature formation. This model can help advance understanding of how bottom currents influence sedimentary processes along continental margins and abyssal plains.

**Key words:** Continental slope, oceanographic processes, bottom currents, mesoscale eddies, internal waves, contourites, South China Sea

## 1. Introduction

Researchers have interpreted contourites as produced by persistent action of bottom currents (e.g., Stow, 2002; Rebesco et al., 2014), which themselves arise from variation in regional quasi-steady water masses (see review in

Rebesco et al., 2014). In recent years, a number of studies have investigated how these quasi-steady oceanographic processes contribute to contourite feature development. Examples include how marine currents at water mass interfaces influence large-scale terrace formation (Preu et al., 2013; Hernández-Molina et al., 2018) and how cascading density currents may influence small-scale bedforms (sediment waves, erosional scours, furrows) (Trincardi et al., 2007; Ribo et al., 2018; Schnyder et al., 2018). Recent research has also highlighted the importance of intermittent oceanographic processes in contourite erosion and deposition including eddies (Hanebuth et al., 2015; Breitzke et al., 2017; Thran et al., 2018; Chen et al., 2019) and internal waves (Reeder et al., 2011; Pomar et al., 2012; Droghei et al., 2016; Ribo et al., 2016; Xie et al., 2018; Zhang et al., 2019). These energetic oceanographic processes occur throughout the world's ocean basins (Shanmugam, 2014; McWilliams, 2016). Their scale and pervasive distribution call for a better understanding of contourite features and how they may arise from oceanographic processes occurring at different spatio-temporal scales (Rebesco et al., 2014; Hernández-Molina et al., 2016).

Different oceanographic processes can contribute to contourite features on local, regional and global scales (e.g., Rebesco et al., 2014; Ribo et al., 2016; Thran et al., 2018), but research has not yet to systematically consider how a diverse set of oceanographic processes interact to influence seafloor at a given locality. The South China Sea represents a natural lab for this sort of inquiry

because it hosts a wide range of major oceanographic processes operating at different spatio-temporal scales, including water exchange with the Pacific (see review in Wang and Li, 2009), powerful internal solitary waves (e.g., Alford et al., 2015), and frequent mesoscale eddies (e.g., Nan et al., 2011). These conditions can elucidate how multiple oceanographic processes interact with the seafloor to generate bottom current (contourite) features. This paper provides novel insights into how oceanographic processes interact with the seafloor at different scales in the northern South China Sea (Fig. 1). The objectives of the study were to (1) describe dominant regional morphological features and document their association, (2) decode spatial and temporal interactions of different oceanographic processes with the seafloor in developing contourite features, and (3) propose a sedimentary model for interpreting interactions as they may occur in other marginal and basinal settings.

## **2. Geological and oceanographic setting**

The South China Sea is one of the largest marginal seas of the western Pacific (Fig. 1). It formed as a result of seafloor spreading during the Oligocene to middle Miocene (33–15 Ma; Taylor and Hayes, 1980; Li et al., 2014) and subsequent eastward subduction along the Manila Trench (Hayes and Lewis, 1984). In the northeastern South China Sea, the Philippine Sea plate's Luzon arc has overridden the South China margin of the Eurasia plate since the latest

Miocene to earliest Pliocene to cause uplift of Taiwan Island (see review in Wang and Li, 2009). Our study area comprises the continental margin of the northern South China Sea (Fig. 1). This margin extends southwest-northeast and reaches water depths of 700–3500 m. It is bounded by the Dongsha Islands in the northwest, the Island of Taiwan in the northeast, and the Luzon Strait to the east. The South China Sea basin opens to the south and southwest. Numerous isolated bathymetric features appear in the study area, including seamounts, highs, and banks (Fig. 1).

The Dongsha Islands region along the upper continental slope was uplifted after seafloor spreading associated with intrusion of magma into the upper crust (e.g., Lüdmann and Wong, 1999; Lüdmann et al., 2001; Wu et al., 2004; Zhao et al., 2012; Xie et al., 2017). This tectonic event occurred from the late Miocene to Pleistocene (e.g., Lüdmann and Wong, 1999; Lüdmann et al., 2001; Wu et al., 2004; Xie et al., 2017). Lüdmann and Wong (1999) initially reported episodic uplift at the Miocene/Pliocene boundary (5.3 Ma) and during the early middle Pleistocene (0.46 Ma). The event caused tilted strata and subaerial erosion of the upper continental slope where consolidated Miocene strata are unconformably overlain by a thinner Pleistocene deposits (Lüdmann et al., 2001).

Modern circulation of the South China Sea is primarily driven by a water exchange with the Pacific Ocean through the Luzon Strait (Fig. 1). The

present-day South China Sea hosts four major water masses (Fig. 2) which include surface, intermediate, deep, and bottom water. The surface water (SW) occurs between 0 and 500 m water depth (wd) in the northern South China Sea and exhibits a density ranging between 1021.0 and 1026.8 kg/m<sup>3</sup> (e.g., Qu et al., 2006; Tian et al., 2006; Zhang et al., 2015). The SW circulation is cyclonic in winter and anticyclonic in summer. The Kuroshio Current influences this circulation such that it becomes more vigorous in winter and during glacial periods (Wang and Li, 2009). With a density between 1026.8 and 1027.55 kg/m<sup>3</sup>, the intermediate water (IW) circulates between ~500 and ~1500 m wd in the northern South China Sea (Tian et al., 2006). This circulation is generally anticyclonic (Tian et al., 2006) although cyclonic circulation may occur during summer (Yang et al., 2010). IW circulation is mostly driven by inflow of the North Pacific Intermediate Water through the Luzon Strait (e.g., Okazaki et al., 2010; Wu et al., 2017). It intensifies during winter months (Tian et al., 2006; Yang et al., 2010) and during glacial periods (Ohkushi et al., 2003; Horikwa et al., 2010; Rella et al., 2012). The deep water (DW) occurs between ~1500 and ~2000 m wd, exhibits a density ranging from 1027.55 to 1027.7 kg/m<sup>3</sup>, and flows in a cyclonic direction (Qu et al., 2006). The DW circulation becomes weaker in winter relative to summer (Tian et al., 2006; Yang et al., 2010; Zhao et al., 2015) and during glacial periods relative to interglacial periods (Wan and Jian, 2014; Zheng et al., 2016; Wan et al., 2018). The bottom water (BW) occurs

at depths below 2000 m wd and exhibits a density typically between 1027.7 and 1027.8 kg/m<sup>3</sup> (Qu et al., 2006; Zhang et al., 2015). Both BW and DW circulation are driven by inflow of Pacific Deep Water through the Luzon Strait. This water consists of North Pacific Deep Water and Upper Circumpolar Deep Water (see review in Wu et al., 2015, 2017). Movement of the BW in the northern South China Sea is typically cyclonic, but the water mass includes two distinct current cores between ~2000 and 2700 m wd (upper core) and between ~2700 and 3000 m wd (lower core) (Tian et al., 2006; Yang et al., 2010). The upper-core (UBW) circulation is anticyclonic while the lower-core (LBW) circulation is cyclonic (Tian et al., 2006; Yang et al., 2010; Zhao et al., 2014). The UBW circulation is more vigorous in winter months relative to summer months (Tian et al., 2006; Yang et al., 2010) and during glacial periods relative to interglacial periods (Wan and Jian, 2014; Zheng et al., 2016; Jian et al., 2018). The LBW circulation is more vigorous in summer months relative to winter months (Tian et al., 2006; Yang et al., 2010) but does not show clear glacial vs. interglacial variation patterns.

In addition to regional water mass circulation, mesoscale eddies (e.g., Wang et al., 2003, 2008; Nan et al., 2011, 2015; Du et al., 2014; Zhang et al., 2017) and internal waves (e.g., Reeder et al., 2011; Alford et al., 2015; Huang et al., 2016) are both common processes in the South China Sea, especially in its northern part. Mesoscale eddies reach diameters between 100 and 160 km and

may persists for 5 to 40 weeks (Nan et al., 2011). Both cyclonic and anticyclonic mesoscale eddies pass through the study area (Nan et al., 2011). These often coexisted in surface waters, but anticyclonic eddies were stronger and lasted longer than cyclonic eddies during some periods, as from October 1992 to October 2009 (Nan et al., 2011). In deeper sea regions, mesoscale eddies are more energetic and occur more often in winter than in summer due to larger density differences between the South China Sea and the Pacific Ocean, and due to faster Pacific inflow (Zhou et al., 2014). Internal waves that originate in the Luzon Strait along the eastern margin of the South China Sea are the largest solitary waves documented in the global oceans (Alford et al., 2015). These waves reach amplitudes of up to 240 m and wavelengths of up to 6 km (Klymak et al., 2006; Huang et al., 2016). They propagate from the Luzon Strait westward at water depths of up to 500 m (Hsu and Lin, 2009). As diurnal processes, internal waves can enhance mixing and increase flow speed of the entire water column (Huang et al., 2016). They are more energetic in winter than in summer (Wang et al., 2011; Huang et al., 2016).

Contourite features in the northern South China Sea include modern contourite drifts, bottom-current formed sediment waves, channels, moats, and terraces (e.g., Lüdmann et al., 2005; Chen et al., 2014, 2016; Gong et al., 2015; Wang et al., 2018). Bottom current activity is also recorded in late Miocene to present day deposition around northwesterly areas of the South China Sea

(Palamenghi et al., 2015). In the study area along-slope sediment transport has clearly evidence since ~3 Ma (Wan et al., 2010; Liu et al., 2017). Contour currents primarily transport clay-sized sediment (Liu et al., 2016) and seismic profiles clearly document resulting contourite drifts and moats (Lüdmann et al., 2005; Shao et al., 2007; Li et al., 2013).

### 3. Data and methods

Multibeam bathymetric data (Fig. 3A) were collected using a SeaBat8150 multibeam bathymetry system, which has a launch frequency of 12 kHz, a maximum coverage angle of 100°, and a spatial resolution of 200 m. The basic morphometric parameters of contourite features (e.g., water depth, trend, length, width, and relief) were measured from the bathymetric data.

This study interprets 17 2-D, multichannel seismic profiles (Fig. 3A). The dominant frequency of the seismic data ranged from 30 to 60 Hz, corresponding to a vertical resolution (tuning thickness) of between 14.2 and 7.1 m. Image processing assumed an average interval velocity of 1700 m/s for the near seafloor interval based on sonic logs from Ocean Drilling Program (ODP) site 1144. The seismic data were processed using a standard pre-stack time-migration procedure. Major processing tasks included denoising, deconvolution, amplitude correction, trace select, normal moveout, velocity analysis, multiple wave suppression, true amplitude stack, and time migration.

In addition to regional seismic stratigraphic analysis, seismic profiles were used to identify sedimentary stacking pattern, perform regional seismic stratigraphic analysis, and document detail of bottom current features. Drill cores from ODP site 1144 (Wang et al., 2000) (Fig. 3A) and piston cores interpreted from literature sources (Yang et al., 2008; Huang et al., 2015) provided constraints on both the chronostratigraphic framework and sedimentary characteristics of the contourite features.

The World Ocean Atlas 2013 dataset with  $0.25^\circ$  spatial resolution for 1955–2012 (<https://odv.awi.de/en/data/ocean/world-ocean-atlas-2013/>) provided regional oceanographic data including annual average salinity and temperature. These data were used to link regional water masses to large contourite features along the margin. Mooring observations at three sites described in literature sources (Zhang et al., 2013; Dong et al., 2015; Zhao et al., 2015) recorded mesoscale eddy and internal wave activity in the study area. This information informed interpretation of sedimentary features that showed spatial and temporal overlap with hydrographic data (Fig. 3A). All three mooring systems were equipped with 75 kHz acoustic doppler current profilers. The M1 observation mooring (Fig. 3A) was installed at 2100 m water depth south of the Dongsha Islands from September 2011 to May 2013 (Zhao et al., 2015). The M2 observation mooring was installed at 2750 m water depth northeast of the Dongsha Islands from April 2011 to March 2012 (Zhao et al., 2013). The M3

observation mooring was installed at 2460 m water depth northeast of the Dongsha Islands from 2 October to 4 October 2012 (Dong et al., 2015).

A 3-D morphodynamic numerical model (Hanebuth et al., 2015; Chen et al., 2016, 2019; Zhang et al., 2016a, 2016b) was used to investigate the theoretical influence of mesoscale eddies on the development of contourite features. The three major functional modules of the model include first, a 3-D circulation module based on the Princeton Ocean Model (Blumberg and Mellor, 1987; Mellor, 2004). This module adopts the fourth-order vertical pressure gradient scheme from McCalpin (1994) to resolve hydrodynamics in response to complex topography with a large bathymetric gradient. The model also used a bottom boundary layer module adopting a quadratic drag relationship (with constant drag coefficient 0.0025) between bottom current velocity and bed shear stress. In addition, the model used a suspended-sediment transport module based on the ECOMSED model (HydroQual, Inc., 2002) in order to calculate resuspension, migration, and deposition of fine-grained sediments (clay/silt/very fine sand). The model reproduced regional oceanic circulation using a nested grid system with coarse grid resolution of  $15 \times 15$  km covering the entire South China Sea and western Pacific Ocean. Resulting quasi-steady geostrophic currents provide open boundary conditions for the higher-resolution grid ( $800 \times 800$  m) that covers our study area (shown in Fig. 3). Results from high-resolution modeling are compared with seismic profiles to assess physical

links between empirical and theoretical datasets. Model specification details are provided in the supplementary material.

## 4. Results

### 4.1 Study area physiography

The eastern part of the northern South China Sea margin includes a wide shelf (140–160 km wide), slope, and rise of varying width. The continental slope divides into upper, middle, and lower slope regions (Fig. 3). The upper slope extends downslope from the shelf break at 125–175 m wd to ~1000 m wd. This zone varies in width (maximum 160 km), exhibits a gentle slope ( $0.2^{\circ}$ – $0.5^{\circ}$ ), and hosts the Dongsha Islands. The middle slope runs downslope from ~1000 m to ~1500 m wd and is characterized by a mean width of 55 km and slope gradient of  $0.1^{\circ}$ – $0.2^{\circ}$ .

The lower slope extends downslope from ~1500 to ~2200 / 2500 m wd. It exhibits a mean width of 65 km and slope gradient of  $1^{\circ}$ – $3^{\circ}$ . Several circular to linear bathymetric features appear in this zone. The two largest of these features are referred to as elevations E1 and E2. E1 is circular and reaches heights of 1765 m and a diameter of 5 km. E2 is a linear feature with an east-west trend. It reaches 783 m in height and extends 29 km in length and 6 km in width.

At ~2200 / 2500 m, the continental slope transitions into the continental rise. The rise exhibits slope gradients of  $1^{\circ}$ – $2^{\circ}$  and hosts prominent bathymetric

features. Of these, the largest (E3 to E10, Fig. 3) occur as linear features averaging 60–1250 m in height, 18–45 km in length, and 4–20 km in width. Two of the features (E3 and E5) strike east-west while the other six (E4, E6–10) strike northeast-southwest (Fig. 3). At ~3000 / 3500 m, the continental rise transitions into the abyssal plain, which is characterized by slope gradients of 0.3°–0.5°.

The seafloor of the study area includes a diverse set of prominent downslope and along-slope features (Fig. 3). Although they are not the focus of this paper, downslope sedimentary features are ubiquitous in the study area. The most prominent downslope features are submarine canyons (Fig. 3). Eight large submarine canyon systems (CS) were numbered sequentially from east to west as CS1–CS8 (Fig. 3). Incision of these features reaches widths of up to 11 km and depths of up to 580 m. Their steepened walls exhibit gradients of 5°–20°. Canyons extend down from the upper or middle slope to the continental rise or abyssal plain. Given this extent, they can reach lengths of up to 150 km.

#### **4.2 Seismic stratigraphic analysis**

Six main seismic units (SU) were identified along the slope. The oldest SU represents a sedimentary package without contourite features (Pre-drift, Figs. 4 and 5). The five succeeding seismic units (SU5 to SU1, from bottom to top) consist primarily of drift deposits and are bound by five regional discontinuities,

labelled H5 to H1 (from bottom to top). These discontinuities are high-amplitude reflections representing erosional surfaces. The H5 discontinuity represents the most important regional unconformity because it overlies the pre-drift unit and lies at the base of all contouritic drifts identified within the study area. Seismic-well-core correlation with ODP site 1144 shows that H5 corresponds to a diminished gamma ray value and a downward lithologic shift from clay to sand (Fig. 6).

H5 also forms the base of the SU5 seismic unit, which is characterised by onlap and downlap reflection terminations, and reflections that are generally low amplitude but high continuity. It forms a regional sheeted body which can be locally mounded with an internal, aggradational configuration (Figs. 4 and 5). Analysis of ODP site 1144 cores indicates that SU5 consists primarily of clays interbedded with thin silts and minor, thinly bedded sands (Fig. 6).

The H4 surface forms the base of SU4 (Figs. 4 and 5). The surface is marked by an increase in p-wave velocity and density, as well as by a downward lithologic shift from clay to silt evident from core material (Fig. 6). SU4 exhibits continuous, moderate amplitude reflections highlighting an aggradational configuration of mounded or sheeted shape (Figs. 4 and 5). ODP site 1144 core material indicates that SU4 consists primarily of clays interbedded with thin silts (Fig. 6).

SU3 is bounded by H3 at its base, a discontinuity that exhibits clear local

erosional truncation (Figs. 4 and 5). Seismic-well-core correlation with ODP site 1144 shows that H3 corresponds to an increase in p-wave velocity and density, diminished gamma ray values, and a depositional hiatus (Fig. 6). Reflections within SU3 onlap onto H3. The internal reflection configuration is aggradational with high amplitude, continuous, reflections that highlight varying sheeted to mounded external forms (Figs. 4 and 5). This seismic unit represents a deposit having a higher acoustic response. Locally disrupted seismic reflection patterns in this unit (Fig. 4C) represent mass transport deposits. The ODP site 1144 core material shows that SU3 consists primarily of clays interbedded with thin silts and sands (Fig. 6).

The H2 surface forms the base of SU2 (Figs. 4 and 5), which shows a hiatus along with increasing p-wave velocity and density (Fig. 6) in ODP site 1144 data. The SU2 reflections onlap onto the H2 surface and exhibit a regional scale aggradational configuration. Continuous, moderate amplitude reflections (Figs. 4 and 5) highlight a mounded or sheeted shape. Core material from ODP site 1144 shows that SU2 consists primarily of clays interbedded with silts (Fig. 6).

The H1 surface forms the base of SU1, the uppermost unit which includes the seafloor. The H1 discontinuity corresponds to a truncation surface characterized by an increase in p-wave velocity and density as well as diminished gamma ray values (Fig. 6). In seismic images, SU1 exhibits

moderate to high amplitude, continuous reflections that onlap onto H1 and highlight an aggradational configuration with mounded to sheeted external forms (Figs. 4 and 5). This unit also hosts local, contorted seismic reflections (Fig. 5A). The ODP site 1144 core materials record primarily clays interbedded with thin silts within this unit (Fig. 6).

All seismic units identified exhibit the same internal seismic facies pattern with transparent or weak facies at their base transitioning progressively upward into high amplitude reflections and terminating in an erosional surface associated with each discontinuity (Figs. 4 and 5). Units SU5 and SU4, and particularly their drifts, exhibit a generally aggradation seismic configuration with weak seismic facies and sheeted forms. SU3, SU2, and SU1 show varying degrees of lateral migration with higher amplitude reflections and more mounded morphologies (Figs. 4 and 5). The H3 discontinuity becomes a regional scale feature due to shifts in reflectivity and morphologies.

#### **4.3 Along-slope features: morphosedimentary and seismic characteristics**

Extensive, along-slope features are common along the entire margin, even where downslope features predominate (Fig. 3). This section classifies the along-slope features as depositional, erosional, and mixed (erosional-depositional).

### 4.3.1 Depositional along-slope features

Depositional along-slope features include sediment drifts and wavy bedforms. Four large drifts (Drifts-1, -2, -3 and -4) occur along the lower continental slope and rise. Drift-1 extends along the lower slope between 1700 and 2200 m wd and occupies a position basinward and adjacent to a submarine terrace in a relatively flat area (Fig. 4A). This drift is crossed by five large submarine canyons and hosts several failure features including slide scarps and slumps (Fig. 3). Drift-1 exhibits a general sheeted shape attached to the slope, being 185 km long, up to 20 km wide, and up to 315 m thick (Fig. 4A). Continuous reflections in Drift-1 highlight aggradational and basinward progradational features (Fig. 4A). Migrating wavy seismic reflections appear near the top of this drift (Fig. 4A).

Drift-2 occurs along the lower slope between 1650 m and 2200 m wd next to Drift-1. Elevations E2 and E3 described above occur on its southeastern flanks (Fig. 3). Drift-2 exhibits a mounded shape with a maximum width of ~17 km and a sedimentary thickness of up to 450 m (Fig. 4C). Seismic lines show upslope progradation of continuous reflections with moderate amplitude (Fig. 4C). Migrating wavy seismic reflections occur near the top of Drift-2 (Fig. 4C). Drift-2 sediment from core material includes dull, grey-green, massive clay intercalated with thin silt and sand layers (Fig. 6, Wang et al., 2000). A piston core (SC2 in this study, Fig. 4C) collected near the foot of Drift-2 also

contained sediment consisting primarily of clays deposited within the last ~25 ka (Huang et al., 2015). The finer-grained (silty) layers and hiatus record interglacial periods (Fig. 6).

Drift-3 occurs along the lower slope to rise and therefore represents a deeper feature than Drift-1 and Drift-2. Located at water depths between ~2250 and 2500 m (Figs. 3), Drift-3 appears along the northwestern flank of isolated E4 and E5 features (Figs. 3, 5A, 5B) or along the western flank of the isolated E1 feature (Fig. 3). This drift exhibits a smooth mounded shape, spans 8.6 km in width, and reaches sedimentary thicknesses of up to 420 m (Fig. 5A, B).

Located between ~2500 and 2800 m wd, Drift-4 represents the deepest drift detected along the rise. It occurs between the linear E7 and E8 features to the east, which extend in a southwestward direction (Figs. 3, 5C). It is also located on the southern flank of the isolated E5 feature to the west (Fig. 3). Drift-4 exhibits a mounded shape, spans a maximum width of 18.5 km and reaches sedimentary thicknesses of up to 420 m (Fig. 5C).

Wavy bedforms appear with Drifts-1 and -2 as fields consisting of 3 to 15 rows of ridges per field (Fig. 3 and Fig. 7A). These bedforms occupy the present seafloor between ~1500 and 2500 m wd but concentrate at around 2000 m wd in areas with a slope gradient between  $1^\circ$  and  $2.5^\circ$ . They are asymmetric in cross section reaching 10 to 80 m in height and 1.2–3.5 km in wavelength width (Fig. 7A, B). They appear to migrate upslope or downslope. Bedforms with the

largest wavelength and the largest wave height appear near ~2000 m wd (Fig. 8). Slope gradients of ridges and troughs found in the bedforms range between 2° and 10°. Most of the bedforms trend in northwest or northeast directions, between ~-60° and 50° with a dominant trend at ~-50° (true north at 0°) (Fig. 8). A few bedforms show trends striking at 70°–80° or ~-80°. Some exhibit thicker upslope and thinner downslope flanks and vice versa (Fig. 7B).

#### 4.3.2 Erosional along-slope features

Erosional along-slope features consist primarily of channels, moats, and furrows (Fig. 3). Two main channels are referred to as CC-1 and CC-2. CC-1 extends along the boundary of the lower slope to the rise at between ~2200 and 2500 m wd (Fig. 3). To the east, CC-1 passes between the E1 and E7 features. To the west, this channel runs along the northern flank of the E9 feature. CC-1 reaches a total length of ~105 km, a width of 10.5 km, and a depth of 85 m. It is split by submarine canyons CS5 and CS6 (Fig. 3). Significant truncations occur beneath the modern floor of this channel, and material infilling the older feature exhibits variable but predominantly low amplitude, layered reflections (Fig. 4B). More obvious truncations occur along the southeast side of the channel floor (Fig. 4B). CC-2 runs along the rise between ~2700 and 3000 m wd (Fig. 3). It traverses the northern flank of the E8 feature to the east and runs between the E6 and E10 features to the west. This channel reaches ~160 km total length, 10

km width, and depths of 230 m. It is split by submarine canyons CS5–CS7.

Material infilling the older CC-2 exhibits layered, low amplitude seismic reflections (Fig. 5C).

Moats, a type of valley associated with mounded drifts, run along the flanks of the circular or linear northeast-southwest trending elevated features within the lower slope and rise (Fig. 3). These reach 5 km in width and depths of 225 m. They commonly develop at 1500 and 2700 m wd between drifts and nearby elevated features. Moats are narrower and shorter than channels CC-1 and CC-2. Moats in the eastern sector of the study area are more abundant and larger than those of the western sector (Fig. 3). Moat infill appears as variable amplitude, layered reflections in seismic profiles (Figs. 4C and 5). The moat between Drift-2 and E2 migrated upslope together with the drift (Fig. 4C). Moats between Drift-3 and the nearby E4 and E5 features, and that between Drift-4 and E7, are stacked vertically. These show no notable lateral migration (Fig. 5).

Furrows are a type of smaller erosional valley that commonly run parallel or slightly oblique to isobaths. Furrows exhibiting northeast-southwest and northwest-southeast trends appear along the lower slope, rise, and abyssal plain at water depths exceeding 1500 m (Fig. 3). These reach widths of up to 1.2 km, lengths of 21 km, and depths of 65 m. They exhibit V-shaped cross sections (Figs. 4A, 5B). Longer and wider furrows commonly run along linear elevations

truncating the underlying seismic reflections (Figs. 3, 4A , 5B).

### 4.3.3 Mixed features

Mixed features include flatter surfaces along the continental slope and irregular depressions. A major surface extending 30–40 km along the middle slope at 1100 m to 1500 m wd is interpreted as a terrace. A horizontal proximal area gradually deepens seaward with a distal slope of about  $<1^\circ$  (Fig. 3). Proximal areas of the terrace represent an erosional surface as indicated by truncated underlying reflections (Fig. 7C).

Irregular depressions span widths of 0.1–10 km (average length of longest and shortest axis) and reach depths of 0.01–1 km. These depressions occur at 1500 to 3000 m wd but are relatively scarce at ~2000 m wd (Fig. 8). Distributed across elevated features, they appear most commonly stacked in groups (Fig. 3). Depressions can exhibit round, oval, linear (northwest-southeast and east-west trending), or compound shapes, and reach depths of up to 250 m. They record varying degrees erosion and deposition. Some are dominated by uneven erosion (Figs. 9A, B) or by deposition due to differences in sedimentation relative to nearby areas (Figs. 9A, C). Others show evidence of mixed erosional and depositional stages (Figs. 7A and 9B). Depression infill appears as layered reflections in seismic profiles (Fig. 7B, C).

#### **4.4 Modelling intermittent oceanographic processes and their impact on the seafloor**

The numerical simulations described here used two different scenarios in order to investigate the influence of intermittent but energetic oceanographic processes on local and regional seafloor morphology of the study area (Zhao et al., 2015). Scenario 1 investigated the impact of surface-generated anticyclonic eddies at depth, while Scenario 2 focused on the impact of bottom-generated cyclonic eddies. Results of both scenarios showed that the maximum bottom current speed occurs at the eddy front and can be further strengthened by bathymetric features such as channels and seamounts (Fig. 10). Both scenarios recorded high shear stress ( $> 0.1$  pa) in zones according to their spatial extent (Fig. 10). Wider zones with higher shear stress normally appeared as a block or slender shaped features located within middle slope terrace areas or along large bathymetric elevations (e.g., seamounts) where along-slope channels or moats appear. The smaller zones exhibited more variable (circular, oval, irregular) shapes and typically appeared around topographic elevations. Oval depressions appeared near smaller zones with higher shear stress (Fig. 10). Simulated flow velocities reached 50 cm/s along contourite channels (e.g., CC-1 and CC-2) and around elevated features in both scenarios (Fig. 10). Figure 11 shows estimates of flow speed at eleven points both inside and outside of five local sub-circular or oval depressions during a mesoscale eddy cycle (45 days). Relative to outside

of the depressions, higher flow speeds ( $>13$  cm/s) occurred inside of the depressions over a longer duration during both an anticyclone and cyclone cycle (Fig. 11). The depressions thus experience high bottom current velocities which enhance erosion of the seafloor. High flow speeds ( $>13$  cm/s) also occurred outside of irregular depressions although over a shorter duration (Fig. 11). Simulation of the near-bottom concentration of suspended sediment when a bottom-generated cyclonic eddy passed through (Scenario 2) showed that silty sediments accumulate along the lower continental slope and the rise near elevated features (Fig. 12). In summary, model results show that intermittent currents can be much faster (50 cm/s) than the modern water mass circulation (e.g.,  $<12$  cm/s for IW, Fig. 2), and are strong enough to remobilize, transport, and deposit sediments.

## 5. Discussion

### 5.1 Age framework

High-resolution stratigraphy from ODP site 1144 data (Bühring et al., 2004) date H1–H5 surfaces at 0.13, 0.3, 0.4, 0.86, and 1.1 Ma respectively (Fig. 6). This means that development of defined contouritic drifts (1 to 4) began at 1.1 Ma. The Taiwan orogeny,  $\sim 280$  km distance from the study area, began closing the interarc bathymetric passages from north to south in the Luzon Strait starting at  $\sim 6.5$  Ma (Huang et al., 2018). As a result, at  $\sim 1.2$  Ma, the Bashi

Channel (Fig. 1) then assumed its present-day general configuration to become the major gateway for water exchange between the South China Sea and the Pacific Ocean (Chen et al., 2015). Consequently, long-term tectonic factors caused a narrower connection between the South China Sea and the Pacific Ocean as well as the resulting increase in velocity of water masses and development of sediment drifts.

The H3 discontinuity (0.4 Ma) represents a prominent shift in sedimentary stacking pattern for the observed drifts, especially Drift-3 and Drift-4 (Figs. 4 and 5). H3 marks the initiation of mounded morphologies and a shift from low to high amplitude reflections in seismic images (Figs. 4 and 5) that coincides with coarser grain size sediment observed from ODP site 1144 core (Fig. 6). This indicates that the H3 discontinuity records a major enhancement in regional currents coeval with interglacial conditions (Fig. 6). Pleistocene uplift of the Dongsha Islands at 0.46 Ma and associated tectonic activity (Lüdmann and Wong, 1999) may have induced these regional and local physiographic changes. Steepening of slopes and local relief for example may have then, along with climatic conditions, affected regional water masses (IW, DW, and BW).

H1, H2, and H4 generally correspond to interglacial periods (Fig. 6). The stratigraphic gap identified at ODP site 1144 (Drift-2) during interglacial marine isotope stage 5.5 by Sarnthein et al. (2013) coincides with the H1 hiatus (Fig. 6). These seismic units do not record regional tectonic changes posited by previous

authors (e.g., Lüdmann and Wong, 1999; Huang et al., 2018). H1, H2, and H4 are thus interpreted as primarily reflecting climatic shifts.

## **5.2 Complex oceanographic processes and their association with contourite features**

Multibeam bathymetric data and seismic images show a hierarchy of primary (drifts, channels, moats, furrows, and terraces) and secondary (wavy bedforms and irregular depressions) features at different scales and depths in the northern South China Sea. The ensuing section interprets these.

### **5.2.1 Classification of contourite drifts and depositional systems**

Drifts-1 through -4, are classified according to the system outlined by Faugères et al. (1999), Fauguères and Stow (2008), and Rebesco et al. (2014). Drift-1 is defined as a plastered drift associated with the adjacent terrace on the middle slope. Drift-2 is defined as a mounded elongated and separated drift based on its prominent mounded shape, up-slope migration, and its association with a moat along the flanks of elevated features E2 and E3. Drift-3 is also defined as a deeper, mounded, elongated and separated drift along the flanks of E1 and E5. Finally, Drift-4 is interpreted as a confined drift based on its distribution between E7 and E8 and the limited extent of its lateral migration.

Depositional (drifts) and erosional (channels, moats, and furrows) contouritic features can be grouped according to water depth and classified as

different contourite depositional system (CDS). We designate contourite depositional system 1 (CDS-1) to include Drift-1 (1700–2200 m wd) and Drift-2 (1650–2200 m wd) along with their associated moats and furrows. A second contourite depositional system (CDS-2) includes Drift-3 (2250–2500 m wd), CC-1 (2200–2500 m wd), and associated moats and furrows. Finally, CDS-3 includes Drift-4 (2500–2800 m wd), CC-2 (2700–3000 m wd), and associated moats and furrows.

## 5.2.2 Contourite depositional systems and regional water masses

### a) *Contourite depositional systems*

CDS-1 occupies the depth range of the Deep Water (DW) mass (1500–2000 m wd) (Fig. 13). The occurrence of Drift-1, Drift-2, and the surrounding moats along the southern side of elevations E2 and E3 indicates that westward, Coriolis-controlled geostrophic flow concentrated along the western side of the ocean basin formed the drifts and moats as evidenced by morphologies, sedimentary directional data, and other observations (Faugères et al., 1999; Hernandez-Molina et al., 2006, 2008; Rebesco et al., 2014). A westward flow direction coincides with regional circulation of the DW in the northern South China Sea (Qu et al., 2006). Under these circumstances, southwesterly areas of Taiwan could provide muddy sediment that formed Drift-2. The regional fine-grained size distribution of sediment supports this

interpretation (Shao et al., 2001; Wan et al., 2010). The plastered nature of Drift-1 implies a weak current regime and low sediment supply during drift formation (Miramontes et al., 2019). The terrace on top of Drift-1, located at ~1500 m wd around the DW and Intermediate Water Mass (IW) boundary, as well as prominent erosional features in proximal areas of the terrace indicate a more vigorous IW relative to the DW. The occurrence of channel CC-1 at the base of Drift-1 records the position of the faster flow of the main UBW core. Drift-1 thus formed in association with weaker flow of the DW. These interpretations resemble those described by Miramontes et al. (2019) for areas of the NW Mediterranean Sea. For this latter study area, a weak current with an estimated velocity of ~7 cm/s and formed between faster cores (>10 cm/s) influenced the observed plastered drift.

The mounded, elongated, and separated Drift-2 indicates a higher bottom current velocity relative to that influencing the adjacent Drift-1. These mounded drifts usually form from water masses with more vigorous currents and higher sedimentation rates (Faugères et al., 1999; Rebesco et al., 2014). Elevated features cause local acceleration to enhance DW flow (Figs. 4 and 13). Our data suggest that along-slope circulation of DW form Drift-1 and the shallower (by ~50 m) Drift-2. Local upwelling of DW and/or BW due to physiography (Lüdmann et al., 2005) or regional uplift during the middle Pleistocene (Lüdmann and Wong, 1999) may have permitted formation of the shallower

feature. Numerical modelling of basin-scale regional water mass circulation in the South China Sea produced upwelling of the DW and BW (Liu and Gan, 2017). Physical evidence of combined DW and BW upwelling only appears in the southern South China Sea however, where along-slope water mass circulation (IW, DW, and BW) ceases at approximately 13°N (Liu and Gan, 2017). The slow speed of upwelling ( $<0.01$  cm/s in average; Liu and Gan, 2017) also does not suffice to form observed contourite features (Stow et al., 2009).

The observed CDS-1 furrows are interpreted to have formed either by the secondary helical flow model (Flood, 1981, 1983; McLean, 1981) or by the flow filament erosion model (García et al. 2009). In the first model, clustered and regularly spaced furrows form due to secondary helical flow at the bottom layer of bottom currents driven by frictional drag along the sea floor (Flood 1981, 1983; McLean 1981). The isolated CDS-1 furrows however do not show the regular spacing suggested by the model (Fig. 3). In the second model, isolated furrows reaching kilometer lengths form in high velocity bottom current settings due to local erosion by flow filaments detached laterally from the mean flow. The model further posits topographic features obstructing and splitting the flow (García et al. 2009; Esentia et al., 2018). The morpho-sedimentary characteristics of furrows in CDS-1 are consistent with features developing in the second model. The occurrence of elongated erosional features is thus attributed to separation of DW current filaments coursing along

linear stretches of elevated topography. Local aggregation and enhancement of water mass filaments can explain the appearance of short furrows around local bathymetric features (Fig. 5B). The CDS-2 and CDS-3 furrows could also arise from erosion by filaments of associated water masses.

CDS-2 forms at water depths (~2500 m) corresponding to the upper core of the bottom water mass (UBW) in the northern South China Sea (Fig. 13). The occurrence of Drift-3 and a moat along the northern flank of elevations E1 and E5 suggest that these features formed under the influence of eastward Coriolis-controlled flow (Faugères et al., 1999; Hernandez-Molina et al., 2006, 2008; Rebesco et al., 2014). Obvious truncations along the southern flank of CC-1 (Fig. 4B) coincide with the position of the current core during eastward flow along the channel. Hydrographic measurements from the eastern portion of the study area found that the UBW flows in an eastward direction at 2000 and 2700 m wd with a present-day velocity of 1–3 cm/s (Fig. 2. Tian et al., 2006; Yang et al., 2010). *In situ* observations along the northern gap of the Luzon Strait also detected eastward flow out of the South China Sea at ~2250 m wd (Zhao et al., 2014), which resembles that of the UBW. CDS-2 thus spatially coincides with Coriolis-controlled UBW circulation. Locally elevated bathymetric features would contribute to increased flow velocity around CDS-2 (Faugères et al., 1999; Llave et al., 2001; Preu et al., 2013). The occurrence of layered channel infill however implies alternation of weaker or more intense

UBW flow.

CDS-3 corresponds to depths (~2700–3000 m) of the lower core of the bottom water mass (LBW) in the northern South China Sea (Fig. 13). The distribution of Drift-4 and the moat along the southern flank of the elevation E7 indicate that Coriolis-driven westward flow influenced formation of this drift and moat (Faugères et al., 1999; Hernandez-Molina et al., 2006, 2008; Rebesco et al., 2014). The LBW's westward flow direction in the northern South China Sea (Tian et al., 2006) supports this interpretation. Formation of CDS-3 is thus attributed to Coriolis-controlled, westward LBW flow locally confined and accelerated by linear elevations E7 and E8. These processes resembled those responsible for forming confined drifts in other areas as well (e.g., Scholl et al., 1977; Reed et al., 1987; Howe et al., 1997).

***b) Contourite terrace***

The middle slope terrace (1100–1500 m wd) forms in association with the IW and DW interface. Hydrographic measurements in the eastern sector of the study area (Figs. 1 and 2) record a boundary between the upper, faster, eastward IW (up to 7–10 cm/s velocity) and the lower, weaker, westward DW (1–3 cm/s velocity) primarily in winter (Tian et al., 2006). This interface may disappear in summer (Yang et al., 2010).

The area around the Dongsha Islands has also been affected twice by late Miocene to Pleistocene uplift (e.g., Lüdmann and Wong, 1999; Lüdmann et al.,

2001; Xie et al., 2017), which may have also contributed to onset of the terrace (Figs. 7C, 13). The terrace has therefore been shaped and maintained by long-term spatial variation in both IW and DW water masses and their interface along the northern margin of the South China Sea. The South China Sea resembles other area in terms of these regional mechanisms (e.g., Hernandez-Molina et al., 2009, 2018; Preu et al., 2013) but local tectonic activity may further enhance certain depositional processes. The data described here indicate that interfaces oriented in a downward direction cause more vigorous IW (Tian et al., 2006; Yang et al., 2010) circulation along the upper slope terrace, which in turn enhances erosional processes. Upward facing interfaces cause a weaker DW to circulate along the terrace and promote deposition.

Mooring observations (M1) from above Drift-2 (Fig. 14A) demonstrate high-energy conditions (up to 10 cm/s) at 1900 m wd induced by mesoscale eddies (Zhang et al., 2014; Zhao et al., 2015) that last for several weeks. Mooring observations from M2 showed that mesoscale eddies enhanced current velocity (up to 5 cm/s) by a factor of about two relative to background conditions at 2525 m wd (Fig. 14B, Zhang et al., 2013; Chen et al., 2015). Our numerical modelling further indicates that mesoscale eddies form faster flows (up to 50 cm/s) that enhance erosion along the contourite terrace and contourite channels and around linear elevations (Figs. 10, 11, 12). Eddies can also

enhance deposition of fine grained sediment in local to regional zones near elevations (Fig. 12). Regional circulation of water masses is therefore affected by intermittent and energetic mesoscale eddies which enhance the local velocity and favour development of primary current-related features.

### **5.2.3 Secondary current-related features and associated processes**

#### **a) Origin of irregular depressions**

Irregular depressions are mixed, smaller-scale secondary features forming along the CDSs during both erosional and depositional stages. When identified in other areas (García et al., 2016; Sun et al., 2017) these features form in association with sediment waves (Symons et al., 2016), pockmarks (Judd and Hovland, 2007), collapse structures, and tectonic activity (Moscardelli and Wood, 2008), or due to other oceanographic process (García et al., 2016). Sediment waves are parallel, linear features that migrate through time (Flood, 1988; Normark et al., 2002; Wynn and Stow, 2002; Symons et al., 2016), but the irregular depressions described herein do not display these basic characteristics (Figs. 5B, 7, 9).

Pockmarks on the sea floor typically exhibit seismic evidence for fluid flow pathways (e.g., pipes and gas chimneys) occurring beneath the depressions (Judd and Hovland, 2007). Seismic profiles show no evidence of these features (Figs. 5B, 7B, 9B, 9C). Collapse structures typically show headscarps, listric

normal faulting around the head, compressional folds around the toe, and glide surfaces (e.g., Hampton et al., 1996; Moscardelli and Wood, 2008; Bull et al., 2009). These diagnostic criteria do not appear around the observed depressions. Tectonic folding can produce linear troughs and ridges that extend perpendicular to regional stress. These large-scale troughs and ridges commonly develop in compressional settings like southwest Taiwan (Chiang et al., 2004; Liu et al., 2004; Lin et al., 2008). The depressions described here are not strictly linear or large (Fig. 3), and they occur primarily within Pleistocene to present day sediment dominated by extensional tectonic activity (Taylor and Hayes, 1980; Lüdmann and Wong, 1999).

Magmatic intrusion took place in widespread areas around the Dongsha Islands during the Quaternary (Lüdmann and Wong, 1999). Irregular depressions appear in association with magmatic features (Fig. 9B, C) indicating a potential association. Depressions are typically larger than underlying intrusive bodies (Fig. 9C) and thus appear to be a primarily sedimentary feature. Non-correspondence between the irregular depressions and the magmatic intrusion in position (Fig. 3) further indicate an alternative origin.

Irregular depressions may originate from interactions between secondary oceanographic processes and the sea floor (García et al., 2016). The shape and size of depressions resembles that of the sub-mesoscale eddies. Sub-mesoscale eddies are generated by the interaction of mesoscale eddy fronts with

bathymetric features produced through energy dipping (McWilliams, 2016). Sub-mesoscale eddies extend to about 0.1–10 km in length (average length of longest and shortest axis) and 0.01–1 km in depth (McWilliams, 2016). Both the irregular depressions (Fig. 3) and sub-mesoscale eddies (McWilliams, 2016; Liu et al., 2017) exhibit predominantly 2-D oval and 3-D conical shapes. Interestingly, axis-asymmetric deposition and erosion of each depression matches the axis-asymmetric structure of the sub-mesoscale eddies (McWilliams, 2016; Zhang et al., 2016; Liu et al., 2017).

The complex topography of the study area provides favourable conditions for generating these sub-mesoscale currents. Numerical modelling of the study area confirmed a clear link between the presence of local depressions on the seafloor, the distribution path of mesoscale eddies, and the formation of sub-mesoscale eddies. These mesoscale eddies induce a higher bottom shear stress in certain areas where the sub-mesoscale eddies are generated and irregular depressions appear (Fig. 10). Modelling shows that sub-mesoscale eddies could induce and maintain higher flow speeds ( $>13$  cm/s) within local depressions relative to surroundings (Fig. 11). Mesoscale eddies also limit the duration of high flow speeds outside of the depressions. As discussed above, these high flow velocities enhance erosion and deposition of the CDSs.

Irregular depressions occur in water depth ranges that overlap that of the DW and the BW (Fig. 8A, B). Very few depressions occur at the exact depth of

the interface between these two water masses. This suggests that sub-mesoscale eddies spread primarily inside regional water masses.

Erosion and deposition within irregular depressions records variation in intensity of the associated current. More vigorous surface and deep mesoscale eddies in winter (Nan et al., 2011; Zhou et al., 2014) cause associated variation in the sub-mesoscale currents, which then cause alternating periods of erosion and deposition.

#### **b) Origin of wavy bedforms**

Wavy bedforms are another secondary feature appearing along the CDSs observed in the study area (Figs. 4, 7A, 7B). Three main mechanisms may contribute to the formation of these features. These mechanisms include gravity-driven sediment creeps or landslides (Stow et al., 1996; Lee and Chough, 2001; Shillington et al., 2012; Pope et al., 2018), turbidity currents (Normark, 1980; Wynn and Stow, 2002), or bottom currents (Flood, 1988; Wynn and Stow, 2002; Rebesco et al., 2014). Sediment creeps would cause increasing fold amplitude or wave relief at depth due to the more intensive folding of deeper, older sediment (Shillington et al., 2012). This diagnostic criteria has not been observed in this study (Figs. 4, 7A, 7B). Layers along ridges/troughs of wavy bedforms dip from  $2^{\circ}$ – $10^{\circ}$  in the study area. These dips are significantly gentler than those observed within and around sediment creeps ( $30^{\circ}$ – $40^{\circ}$ , Shillington et

al., 2012). Distinct headscarps, prominent features of landslide-induced bedforms (Pope et al., 2018), are also absent around wavy bedforms.

Sediment waves influenced by turbidity currents usually appear over wide areas around the mouth of canyons/channels and/or along canyon/channel banks, where they are associated with widespread, unconfined supercritical turbidity currents (e.g., Normark, 1980; Kuang et al., 2014; Yin et al., 2015; Symons et al., 2016). Wavy bedforms on primary CDSs in the study area instead concentrate in water depth ranges that coincide with the water mass interface between the DW and BW (Fig. 8A, B). We therefore interpret them as arising from internal solitary waves propagating and amplified along interfaces between two water masses (Santek and Winguth, 2007; Pomar et al., 2012).

Internal waves can generate muddy- or sandy-dominated sediment waves (Karl et al., 1986; Reeder et al., 2011; Droghei et al., 2016; Ribo et al., 2016). Wave-fronts of westward-propagating internal solitary waves and their eastward-propagating reflections generally trend between  $-60^\circ$  and  $50^\circ$  (from Hsu and Liu, 2000; Wang et al., 2011). These orientations match those observed for most of the wavy bedforms (Fig. 7E). A few wavy bedforms that do not show this trend may arise from refraction (Fett and Rabe, 1977; Zhao et al., 2008; Li et al., 2013) and reflection (Hsu and Liu, 2000; Shaw et al., 2009; Zhang et al., 2011) of internal solitary waves due to sea floor interactions.

Upslope and downslope migration of wavy bedforms (Fig. 7B) indicate

that bedforms form in response to currents moving in opposite directions. The westward-propagating internal solitary waves of depression (i.e., wave with predominantly downward displacement; Hsu and Liu, 2000; Huang et al., 2016) could generate eastward currents in the bottom boundary layer (Boegman and Stastna, 2019) to create opposite downslope near-bed currents. Reflected eastward-propagating internal solitary waves of depression (Hsu and Liu, 2000; Zhang et al., 2011) could generate westward bottom layer currents (Boegman and Stastna, 2019) to create upslope near-bed currents.

Mooring-based current-velocity observations from station M3 (Fig. 14C modified from Dong et al., 2015) in the north of the study area found that internal solitary waves can increase background flow velocity to more than 10 cm/s at ~2374 m wd. According to Stow et al. (2009), a velocity of 10 cm/s can generate fine-grained (muddy) sediment waves. The current velocity necessary to form muddy sediment waves must exceed  $f/k$  (Flood, 1988; Blumsack and Weatherly, 1989), where  $k$  is the wave number defined as  $k = 2\pi/L$  ( $L$  is the sediment wavelength), and  $f$  is the Coriolis parameter defined as  $f = 2\Omega \sin(\theta)$ , with  $\Omega$  being the Earth's rotation rate and  $\theta$  being the latitude ( $20^\circ$  for the study area). For  $L = 3.5$  km, the critical velocity is  $>3$  cm/s. Observed current velocity at 2374 wd exceeds 3 cm/s. Internal wave-generated bottom currents in the study area are thus vigorous enough to form the observed sediment waves.

Winter internal wave velocity exceeds that observed during the summer due

to the way in which a stronger Kuroshio Current helps stratify flow of the Luzon Strait. This triggers more energetic internal waves with larger amplitudes (Wang et al., 2011; Huang et al., 2016). A piston core (SC1, Fig. 4C) sampling upper layers of Drift-2 shows that <30 ka sediment within sediment waves consists primarily of silts. Grain size coarsens however around 20 ka (the last glacial maximum; Yang et al., 2008). This shift could indicate enhanced bottom currents by internal waves during the last glacial stage. Wang and Li (2009) report evidence of a more vigorous Kuroshio Current during glacial periods. This interpretation supports other evidence of more energetic internal waves during sediment wave formation.

The muddy sediment waves described here are larger and deeper than other waves interpreted to have formed from internal waves (Ribo et al., 2016). The more energetic internal waves observed in the study area offer an explanation for this contrast (Alford et al., 2015; Dong et al., 2015; Huang et al., 2016).

The complexity of local bathymetric features also contributes to higher internal wave velocities (Figs. 3 and 7B; Lüdmann and Wong, 1999), as do mesoscale eddies and internal waves (Xie et al., 2015; Dong et al., 2016). Intermittent mesoscale eddies and internal waves coexist in the study area (e.g., Nan et al., 2011; Alford et al., 2015; Dong et al., 2015; Zhang et al., 2017). These two oceanographic processes interact to amplify internal wave amplitudes (Xie et al., 2015) and generate secondary internal waves (Xie et al., 2015). Due

to their novelty, future studies should address these interactions and their influence on deep-sea secondary morphological bottom current features such as the sediment waves and irregular depressions described here.

### **5.3 Sedimentary model**

A sedimentary model is proposed to explain how primary and secondary contourite features develop in association with climatic variation and temporally variable oceanographic processes along the continental margin of the northern South China Sea (Fig. 15).

#### ***Cold periods***

During cold periods (glacial stages), a vigorous northeastward Intermediate Water mass (IW) circulated (Ohkushi et al., 2003; Horikawa et al., 2010; Rella et al., 2012) along the middle slope terrace (Fig. 15). Deposition of muddy plastered Drift-1 and mounded Drift-2 took place along the lower slope (CDS-1) under the influence of a weak southwestward Deep Water mass (DW) (Wan and Jian, 2014; Zheng et al., 2016; Wan et al., 2018). Vigorous northeastward UBW circulation (Wan and Jian, 2014; Zheng et al., 2016; Jian et al., 2018) favoured coarser-grained deposition of mounded Drift-3 and dominant erosional processes within channel CC-1 along the lower slope and rise (CDS-2). Weakened southwestward LBW circulation contributed to muddy deposition along the confined Drift-4 and within channel CC-2 along the rise (CDS-3).

Vigorous shallow anticyclonic and deep cyclonic mesoscale eddies (Nan et al., 2011; Zhou et al., 2014) enhanced local velocities of regional water masses. Eddies and sub-mesoscale eddies within the DW and BW interacted with seabed to generate irregular depressions along eddy paths (Figs. 10, 11, 15). During cold periods, energetic internal waves with larger amplitudes (Wang et al., 2011; Huang et al., 2016) tending to spread along water mass interfaces formed sediment waves.

### *Warm periods*

During warm periods (interglacial stages), weak northeastward IW (Ohkushi et al., 2003; Horikawa et al., 2010; Rella et al., 2012) circulation favoured deposition along the middle slope terrace (Fig. 15). The DW drove circulation towards the southwest (Sarnthein et al., 2013; Wan and Jian, 2014; Zheng et al., 2016; Jian et al., 2018) along CDS-1 of the lower slope. Weak northeastward UBW circulation (Wan and Jian, 2014; Zheng et al., 2016; Jian et al., 2018) caused muddy deposition on Drift-3 and sedimentary infilling of the CC-1 channel along the lower slope and rise (CDS-2). Enhanced southwestward LBW circulation favoured coarser-grained deposition along Drift-4 and erosion processes along channel CC-2 of the rise (CDS-3).

Over the same period, generally weaker mesoscale eddies did not amplify regional water mass circulation. Irregular depressions then experienced deposition (Fig. 15). Internal waves were less frequent and weaker so that

muddy sediment accumulated on sediment waves.

## 6. Conclusions

Deep marine sedimentary features record complex spatio-temporal interactions of primary and secondary sedimentary processes. This study describes multiscale oceanographic processes that form contourite features in the northern South China Sea. Regional water mass circulation forms primary contourite features including contourite depositional systems (CDS) at different depths related to specific water masses (IW, DW, and BW) and their associated interfaces. Water masses exhibit quasi-steady processes with intermittent enhanced or weakened currents due to climatic and seasonal variation. Colder or warmer conditions (glacial vs. interglacial stages) exert long-term influence on the strength and depth of these water masses.

Atmospheric forcing can also generate intermittent, higher energy processes, such as eddies and internal waves. These in turn produce smaller, secondary contourite features within CDSs. Mesoscale eddies can enhance regional water masses and trigger sub-mesoscale (1–10 km) eddies when interacting with seafloor irregularities. These interactions can generate irregular depressions along eddy paths. Internal waves mainly channelized through water mass interfaces, or by bathymetric interactions, generate fields of large sediment waves.

This study used numerical modelling results to interpret primary and secondary contourite features in terms of a hierarchy of sedimentary processes caused by complex spatio-temporal variation in oceanographic processes. This sort of multidisciplinary approach can help further elucidate the role of bottom currents in shaping continental margins and associated sedimentary deposits.

### **Acknowledgements**

We thank Second Institute of Oceanography, Ministry of Natural Resources of China for permission to use and publish multibeam bathymetric data. We also thank Guangzhou Marine Geological Survey and China National Offshore Oil Corporation for permission to use and publish 2-D multichannel seismic profiles. The research was conducted within the framework of “*The Drifters Research Group*” of the Royal Holloway University of London (UK) and is related to projects CTM 2012-39599-C03, CGL2016-80445-R, and CTM2016-75129-C3-1-R. This work was also supported by the National Program on Global Change and Air-Sea Interaction, SOA, under Grants GASI-GEOGE-05 and GASI-GEOGE-01, and the National Natural Science Foundation of China Grant 41706043. The study received additional support from the research programme “Marine, Coastal and Polar Systems” (PACES II) of the Hermann von Helmholtz-Gemeinschaft Deutscher Forschungszentren e.V. The first author thanks Prof. Guangfa Zhong for his guidance on seismic interpretation during the first author’s doctoral studies.

## References

- Alford, M.H. et al., 2015. The formation and fate of internal waves in the South China Sea. *Nature*, 521(7550), 65–69.
- Blumberg, A.F. and Mellor, G.L., 1987. A description of a three-dimensional coastal ocean circulation model. In: Heaps, N.S. (Ed.), *Three-dimensional Coastal Ocean Models*, vol. 4. American Geophysical Union, Washington, DC, pp. 1–16.
- Blumsack, S. L. and Weatherly, G. L., 1989. Observations of the nearby flow and a model for the growth of mudwaves. *Deep Sea Research Part A. Oceanographic Research Papers*, 36(9), 1327–1339.
- Boegman, L. and Stastna, M., 2019. Sediment resuspension and transport by internal solitary waves. *Annual Review of Fluid Mechanics*, 51, 129–154.
- Breitzke, M., Wiles, E., Krockner, R., Watkeys, M.K. and Jokat, W., 2017. Seafloor morphology in the Mozambique Channel: evidence for long-term persistent bottom-current flow and deep-reaching eddy activity. *Marine Geophysical Research*, 38(3), 241–269.
- Bühring, C., Sarnthein, M. and Erlenkeuser, H., 2004. Toward a high-resolution stable isotope stratigraphy of the last 1.1 my: Site 1144, South China Sea, *Proc. ODP, Sci. Results*, pp. 1–29.
- Bull, S., Cartwright, J. and Huuse, M., 2009. A review of kinematic indicators

- from mass-transport complexes using 3D seismic data. *Marine and Petroleum Geology*, 26(7), 1132–1151.
- Chen, H., Xie, X., Van Rooij, D., Vandorpe, T., Su, M. and Wang, D., 2014. Depositional characteristics and processes of alongslope currents related to a seamount on the northwestern margin of the Northwest Sub-Basin, South China Sea. *Marine Geology*, 355, 36–53.
- Chen, H. et al., 2016. Deep-water sedimentary systems and their relationship with bottom currents at the intersection of Xisha Trough and Northwest Sub-Basin, South China Sea. *Marine Geology*, 378, 101–113.
- Chen, H., Zhang, W., Xie, X. and Ren, J., 2019. Sediment dynamics driven by contour currents and mesoscale eddies along continental slope: A case study of the northern South China Sea. *Marine Geology*, 409, 48–66.
- Chen, W. H., Huang, C. Y., Lin, Y. J., Zhao, Q., Yan, Y., Chen, D., ... & Yu, M., 2015. Depleted deep South China Sea  $\delta^{13}\text{C}$  paleoceanographic events in response to tectonic evolution in Taiwan–Luzon Strait since Middle Miocene. *Deep Sea Research Part II: Topical Studies in Oceanography*, 122, 195–225.
- Chiang, C. S., Yu, H. S. and Chou, Y. W., 2004. Characteristics of the wedge-top depozone of the southern Taiwan foreland basin system. *Basin Research*, 16(1), 65–78.
- Dong, J. et al., 2015. Asymmetry of internal waves and its effects on the

- ecological environment observed in the northern South China Sea. *Deep Sea Research Part I: Oceanographic Research Papers*, 98, 94–101.
- Dong, D., Yang, X., Li, X. and Li, Z., 2016. SAR observation of eddy-induced mode-2 internal solitary waves in the South China Sea. *IEEE Transactions on Geoscience and Remote Sensing*, 54(11), 6674–6686.
- Droghei, R. et al., 2016. The role of Internal Solitary Waves on deep-water sedimentary processes: the case of up-slope migrating sediment waves off the Messina Strait. *Scientific Reports*, 6(1).
- Esentia, I., Stow, D., Smillie, Z., 2018. Contourite Drifts and Associated Bedforms. In: A. Micallef, S. Krastel, A. Savini (Eds.), *Submarine Geomorphology*. Springer International Publishing, Cham, pp. 301–331.
- Faugères, J.-C. and Stow, D., 2008. Contourite drifts: nature, evolution and controls. *Developments in sedimentology*, 60, 257–288.
- Faugères, J.C., Stow, D.A.V., Imbert, P. and Viana, A., 1999. Seismic features diagnostic of contourite drifts. *Marine Geology*, 162(1), 1–38.
- Flood, R. D., 1981. Distribution, morphology, and origin of sedimentary furrows in cohesive sediments, Southampton Water. *Sedimentology*, 28(4), 511–529.
- Flood, R. D., 1983. Classification of sedimentary furrows and a model for

- furrow initiation and evolution. *Geological Society of America Bulletin*, 94(5), 630–639.
- Flood, R. D., 1988. A lee wave model for deep-sea mudwave activity. *Deep Sea Research Part A. Oceanographic Research Papers*, 35(6), 973–983.
- García, M., Hernández-Molina, F. J., Llave, E., Stow, D. A. V., León, R., Fernández-Puga, M. C., ... & Somoza, L., 2009. Contourite erosive features caused by the Mediterranean Outflow Water in the Gulf of Cadiz: Quaternary tectonic and oceanographic implications. *Marine Geology*, 257(1–4), 24–40.
- García, M., Hernández-Molina, F. J., Alonso, B., Vázquez, J. T., Ercilla, G., Llave, E. and Casas, D., 2016. Erosive sub-circular depressions on the Guadalquivir Bank (Gulf of Cadiz): interaction between bottom current, mass-wasting and tectonic processes. *Marine Geology*, 378, 5–19.
- Gong, C., Wang, Y., Xu, S., Pickering, K. T., Peng, X., Li, W. and Yan, Q., 2015. The northeastern South China Sea margin created by the combined action of down-slope and along-slope processes: Processes, products and implications for exploration and paleoceanography. *Marine and Petroleum Geology*, 64, 233–249.
- Grant, W.D. and Madsen, O.S., 1979. Combined wave and current interaction with a rough bottom. *Journal of Geophysical Research* 84, 1797–1808.
- Hampton, M. A., Lee, H. J. and Locat, J., 1996. Submarine landslides. *Reviews*

of geophysics, 34(1), 33–59.

- Hanebuth, T.J., Zhang, W., Hofmann, A.L., Löwemark, L.A. and Schwenk, T., 2015. Oceanic density fronts steering bottom-current induced sedimentation deduced from a 50 ka contourite-drift record and numerical modeling (off NW Spain). *Quaternary Science Reviews*, 112, 207–225.
- Hernández-Molina, F., Larter, R., Rebesco, M. and Maldonado, A., 2006. Miocene reversal of bottom water flow along the Pacific Margin of the Antarctic Peninsula: stratigraphic evidence from a contourite sedimentary tail. *Marine Geology*, 228(1), 93–116.
- Hernández-Molina, F., Maldonado, A. and Stow, D., 2008. Abyssal plain contourites. *Developments in Sedimentology*, 60, 345–378.
- Hernández-Molina, F.J. et al., 2018. Large bedforms on contourite terraces: Sedimentary and conceptual implications. *Geology*, 46(1), 27–30.
- Hernández-Molina, F.J. et al., 2016. A contourite depositional system along the Uruguayan continental margin: Sedimentary, oceanographic and paleoceanographic implications. *Marine Geology*, 378, 333–349.
- Horikawa, K., Asahara, Y., Yamamoto, K. and Okazaki, Y., 2010. Intermediate water formation in the Bering Sea during glacial periods: Evidence from neodymium isotope ratios. *Geology*, 38(5), 435–438.
- Howe, J. A., Pudsey, C. J. and Cunningham, A. P., 1997. Pliocene-Holocene

contourite deposition under the Antarctic circumpolar current, western Falkland trough, South Atlantic Ocean. *Marine Geology*, 138(1–2), 27–50.

Hsu, M.-K. and Liu, A.K., 2000. Nonlinear internal waves in the South China Sea. *Canadian Journal of Remote Sensing*, 26(2), 72–81.

Huang, C. Y., Chen, W. H., Wang, M. H., Lin, C. T., Yang, S., Li, X., ... & Hsieh, Y. H., 2018. Juxtaposed sequence stratigraphy, temporal-spatial variations of sedimentation and development of modern-forming forearc Lichi Mélange in North Luzon Trough forearc basin onshore and offshore eastern Taiwan: An overview. *Earth-science reviews*, 182, 102–140.

Huang, E. et al., 2015. Early interglacial carbonate-dilution events in the South China Sea: Implications for strengthened typhoon activities over subtropical East Asia. *Quaternary Science Reviews*, 125, 61–77.

Huang, X. et al., 2016. An extreme internal solitary wave event observed in the northern South China Sea. *Scientific Reports*, 6.

HydroQual, Inc, 2002. A Primer for ECOMSED Version 1.3. (Computer Program Manual). HydroQual, Inc, Mahwah, New Jersey.

Judd, A., Hovland, M., 2007. Seabed Fluid Flow. Cambridge University Press, Cambridge. 475pp.

Karl, H., Cacchione, D. and Carlson, P., 1986. Internal-wave currents as a

- mechanism to account for large sand waves in Navarinsky Canyon head, Bering Sea. *Journal of Sedimentary Research*, 56(5), 706–714.
- Klymak, J.M., Pinkel, R., Liu, C.T., Liu, A.K. and David, L., 2006. Prototypical solitons in the South China Sea. *Geophysical Research Letters*, 35(11).
- Kuang, Z., Zhong, G., Wang, L., and Guo, Y., 2014, Channel-related sediment waves on the eastern slope offshore Dongsha Islands, northern South China Sea: *Journal of Asian Earth Sciences*, 79, 540–551.
- Lee, S.H., and Chough, S.K., 2001, High - resolution (2–7 kHz) acoustic and geometric characters of submarine creep deposits in the South Korea Plateau, East Sea: *Sedimentology*, 48, 629–644.
- Li, C.F. et al., 2014. Ages and magnetic structures of the South China Sea constrained by deep tow magnetic surveys and IODP Expedition 349. *Geochemistry, Geophysics, Geosystems*, 15(12), 4958–4983.
- Li, H., Wang, Y., Zhu, W., Xu, Q., He, Y., Tang, W., ... & Li, D., 2013. Seismic characteristics and processes of the Plio-Quaternary unidirectionally migrating channels and contourites in the northern slope of the South China Sea. *Marine and Petroleum Geology*, 43, 370–380.
- Lin, A. T., Liu, C. S., Lin, C. C., Schnurle, P., Chen, G. Y., Liao, W. Z. and Wu, M. S., 2008. Tectonic features associated with the overriding of an accretionary wedge on top of a rifted continental margin: an example from Taiwan. *Marine Geology*, 255(3–4), 186–203.

- Lisiecki, L.E. and Raymo, M.E., 2005. A Pliocene-Pleistocene stack of 57 globally distributed benthic  $\delta^{18}\text{O}$  records. *Paleoceanography*, 20(1).
- Liu, C. S., Deffontaines, B., Lu, C. Y. and Lallemand, S., 2004. Deformation patterns of an accretionary wedge in the transition zone from subduction to collision offshore southwestern Taiwan. *Marine Geophysical Researches*, 25(1–2), 123–137.
- Liu, J., Steinke, S., Vogt, C., Mohtadi, M., De Pol-Holz, R. and Hebbeln, D., 2017. Temporal and spatial patterns of sediment deposition in the northern South China Sea over the last 50,000 years. *Palaeogeography, Palaeoclimatology, Palaeoecology*, 465, 212–224.
- Liu, L., Silver, D., Bemis, K., Kang, D. and Curchitser, E., 2017. Illustrative Visualization of Mesoscale Ocean Eddies, *Computer Graphics Forum*. Wiley Online Library, pp. 447–458.
- Liu, Z., Zhao, Y., Colin, C., Stattegger, K., Wiesner, M. G., Huh, C. A., and Huang, C. Y., 2016. Source-to-sink transport processes of fluvial sediments in the South China Sea. *Earth-Science Reviews*, 153, 238–273.
- Liu, Z. and Gan, J., 2017. Three- dimensional pathways of water masses in the South China Sea: A modeling study. *Journal of Geophysical Research: Oceans*, 122(7), 6039–6054.
- Llave, E. et al., 2001. Seismic stacking pattern of the Faro-Albufeira contourite

- system (Gulf of Cadiz): a Quaternary record of paleoceanographic and tectonic influences. *Marine Geophysical Researches*, 22(5), 487–508.
- Lüdmann, T. and Wong, H. K., 1999. Neotectonic regime on the passive continental margin of the northern South China Sea. *Tectonophysics*, 311(1–4), 113–138.
- Lüdmann, T., Wong, H. K. and Wang, P., 2001. Plio–Quaternary sedimentation processes and neotectonics of the northern continental margin of the South China Sea. *Marine Geology*, 172(3–4), 331–358.
- Lüdmann, T., Wong, H.K. and Berglar, K., 2005. Upward flow of North Pacific Deep Water in the northern South China Sea as deduced from the occurrence of drift sediments. *Geophysical Research Letters*, 32(5), 1–4.
- McCalpin, J., 1994. A comparison of second-order and fourth-order pressure gradient algorithms in a s-coordinate ocean model. *International Journal for Numerical Methods in Fluids* 18, 361–383.
- McLean, S. R., 1981. The role of non-uniform roughness in the formation of sand ribbons. *Marine Geology*, 42(1–4), 49–74.
- McWilliams, J.C., 2016. Submesoscale currents in the ocean, *Proc. R. Soc. A.* The Royal Society, pp. 20160117.
- Mellor, G., 2004. Users Guide for a Three-dimensional, Primitive Equation, Numerical Ocean Model. Technical Report. Princeton University.

- Miramontes, E., Garreau, P., Caillaud, M., Jouet, G., Pellen, R., Hernández-Molina, F. J. and Cattaneo, A., 2019. Contourite distribution and bottom currents in the NW Mediterranean Sea: Coupling seafloor geomorphology and hydrodynamic modelling. *Geomorphology*, 333, 43–60.
- Moscardelli, L. and Wood, L., 2008. New classification system for mass transport complexes in offshore Trinidad. *Basin research*, 20(1), 73–98.
- Nan, F. et al., 2011. Oceanic eddy formation and propagation southwest of Taiwan. *Journal of Geophysical Research: Oceans*, 116(C12).
- Normark, W. R., Hess, G. R., Stow, D. A. V. and Bowen, A. J., 1980. Sediment waves on the Monterey Fan levee: a preliminary physical interpretation. *Marine Geology*, 37(1–2), 1–18.
- Normark, W. R., Piper, D. J., Posamentier, H., Pirmez, C. and Migeon, S., 2002. Variability in form and growth of sediment waves on turbidite channel levees. *Marine Geology*, 192(1–3), 23–58.
- Ohkushi, K.i., Itaki, T. and Nemoto, N., 2003. Last Glacial–Holocene change in intermediate-water ventilation in the Northwestern Pacific. *Quaternary Science Reviews*, 22(14), 1477–1484.
- Okazaki, Y. et al., 2010. Deepwater formation in the North Pacific during the Last Glacial Termination. *329(5988)*, 200–204.
- Pomar, L., Morsilli, M., Hallock, P. and Bádenas, B., 2012. Internal waves, an

- under-explored source of turbulence events in the sedimentary record. *Earth-Science Reviews*, 111(1), 56–81.
- Pope, E. L., Jutzeler, M., Cartigny, M. J., Shreeve, J., Talling, P. J., Wright, I. C. and Wysoczanski, R. J., 2018. Origin of spectacular fields of submarine sediment waves around volcanic islands. *Earth and Planetary Science Letters*, 493, 12–24.
- Preu, B. et al., 2013. Morphosedimentary and hydrographic features of the northern Argentine margin: the interplay between erosive, depositional and gravitational processes and its conceptual implications. *Deep Sea Research Part I: Oceanographic Research Papers*, 75, 157–174.
- Qu, T., Girton, J.B. and Whitehead, J.A., 2006. Deepwater overflow through Luzon strait. *Journal of Geophysical Research: Oceans*, 111(C1).
- Rebesco, M., Hernández-Molina, F.J., Van Rooij, D. and Wåhlin, A., 2014. Contourites and associated sediments controlled by deep-water circulation processes: State-of-the-art and future considerations. *Marine Geology*, 352(0), 111–154.
- Reed, D. L., Meyer, A. W., Silver, E. A. and Prasetyo, H., 1987. Contourite sedimentation in an intraoceanic forearc system: eastern Sunda Arc, Indonesia. *Marine Geology*, 76, 223–241.
- Reeder, D.B., Ma, B.B. and Yang, Y.J., 2011. Very large subaqueous sand dunes on the upper continental slope in the South China Sea generated by

- episodic, shoaling deep-water internal solitary waves. *Marine Geology*, 279(1), 12–18.
- Rella, S.F. et al., 2012. Abrupt changes of intermediate water properties on the northeastern slope of the Bering Sea during the last glacial and deglacial period. *Paleoceanography*, 27(3).
- Ribó, M. et al., 2018. Large sediment waves over the Gulf of Roses upper continental slope (NW Mediterranean). *Marine Geology*, 399, 84–96.
- Ribó, M. et al., 2016. Morphobathymetric analysis of the large fine-grained sediment waves over the Gulf of Valencia continental slope (NW Mediterranean). *Geomorphology*, 253, 22–37.
- Santek, D. and Winguth, A., 2007. A satellite view of internal waves induced by the Indian Ocean tsunami. *International Journal of Remote Sensing*, 28(13–14), 2927–2936.
- Schnyder, J.S. et al., 2018. Morphometric analysis of plunge pools and sediment wave fields along western Great Bahama Bank. *Marine Geology*, 397, 15–28.
- Scholl, D. W., Hein, J. R., Marlow, M. and Buffington, E. C., 1977. Meiji sediment tongue: North Pacific evidence for limited movement between the Pacific and North American plates. *Geological Society of America Bulletin*, 88(11), 1567–1576.
- Shanmugam, G., 2013. Modern internal waves and internal tides along oceanic

- pycnoclines: Challenges and implications for ancient deep-marine baroclinic sands. *AAPG bulletin*, 97(5), 799–843.
- Shanmugam, G. and Wang, Y., 2014. Review of research in internal-wave and internal-tide deposits of China: Discussion. *Journal of Palaeogeography*, 3(4), 332–350.
- Shao, L., Li, X., Wei, G., Liu, Y. and Fang, D., 2001. Provenance of a prominent sediment drift on the northern slope of the South China Sea. *Science in China Series D: Earth Sciences*, 44(10), 919.
- Shao, L., Li, X., Geng, J., Pang, X., Lei, Y., Qiao, P., ... & Wang, H., 2007. Deep water bottom current deposition in the northern South China Sea. *Science in China Series D: Earth Sciences*, 50(7), 1060–1066.
- Shillington, D.J., Seeber, L., Sorlien, C.C., Steckler, M.S., Kurt, H., Dondurur, D., Cifci, G., Imren, C., Cormier, M.H., and McHugh, C., 2012, Evidence for widespread creep on the flanks of the Sea of Marmara transform basin from marine geophysical data: *Geology*, 40, 439–442.
- Sun, Q., Cartwright, J., Lüdmann, T., Wu, S. and Yao, G., 2017. Three - dimensional seismic characterization of a complex sediment drift in the South China Sea: Evidence for unsteady flow regime. *Sedimentology*, 64(3), 832–853.
- Stow, D., Reading, H., and Collinson, J., 1996, Deep seas, in H.G. Reading, eds., *Sedimentary environments: processes, facies and stratigraphy*,

- Blackwell Science, 395–453.
- Stow, D.A.V., 2002. Deep-water contourite systems: modern drifts and ancient series, seismic and sedimentary characteristics. Geological Society Pub House.
- Stow, D. A., Hernández-Molina, F. J., Llave, E., Sayago-Gil, M., Díaz del Río, V. and Branson, A., 2009. Bedform-velocity matrix: the estimation of bottom current velocity from bedform observations. *Geology*, 37(4), 327–330.
- Symons, W. O., Sumner, E. J., Talling, P. J., Cartigny, M. J. and Clare, M. A., 2016. Large-scale sediment waves and scours on the modern seafloor and their implications for the prevalence of supercritical flows. *Marine Geology*, 371, 130–148.
- Taylor, B. and Hayes, D.E., 1980. The tectonic evolution of the South China Basin. *Geophysical Monograph Series*, 23, 89–104.
- Thran, A.C., Dutkiewicz, A., Spence, P. and Müller, R.D., 2018. Controls on the global distribution of contourite drifts: Insights from an eddy-resolving ocean model. *Earth and Planetary Science Letters*, 489, 228–240.
- Tian, J. et al., 2006. Observation of Luzon Strait transport. *Geophysical Research Letters*, 33(19).
- Trincardi, F., Verdicchio, G. and Miserocchi, S., 2007. Seafloor evidence for the interaction between cascading and along - slope bottom water masses.

- Journal of Geophysical Research: Earth Surface, 112(F3).
- Wan, S., Li, A., Clift, P. D., Wu, S., Xu, K. and Li, T., 2010. Increased contribution of terrigenous supply from Taiwan to the northern South China Sea since 3 Ma. *Marine Geology*, 278(1–4), 115–121.
- Wan, S. and Jian, Z., 2014. Deep water exchanges between the South China Sea and the Pacific since the last glacial period. *Paleoceanography*, 29(12), 1162–1178.
- Wan, S., Jian, Z. and Dang, H., 2018. Deep Hydrography of the South China Sea and Deep Water Circulation in the Pacific Since the Last Glacial Maximum. *Geochemistry, Geophysics, Geosystems*, 19(5), 1447–1463.
- Wang, P., W. L. Prell, and P. Blum, 2000, Proceedings of the Ocean Drilling Program, Initial Reports: Ocean Drilling Program, 184, 566.
- Wang, P., and Li, Q., 2009, *The South China Sea: Paleoceanography and Sedimentology*: Springer, 506p.
- Wang, J., Huangb, W., Yangb, J. and Zhangb, H., 2011. The internal waves' distribution of whole South China Sea extracted from ENVISAT and ERS-2 SAR images, *Proc. of SPIE Vol*, pp. 81751G-1.
- Wang, X., Zhuo, H., Wang, Y., Mao, P., He, M., Chen, W. and Wang, M., 2018. Controls of contour currents on intra-canyon mixed sedimentary processes: Insights from the Pearl River Canyon, northern South China Sea. *Marine Geology*, 406, 193–213.

- Wu, Q. et al., 2017. Foraminiferal  $\epsilon\text{Nd}$  in the deep north-western subtropical Pacific Ocean: Tracing changes in weathering input over the last 30,000years. *Chemical Geology*, 470(Supplement C), 55–66.
- Wu, S. et al., 2004. Late Cenozoic Neotectonics in the Donsha Islands region and its response to collision between Chinese continental margin and Luzon. *Oceanologia Etlimnologia Sinica*, 35, 481–490 (in Chinese).
- Wynn, R. B. and Stow, D. A., 2002. Classification and characterisation of deep-water sediment waves. *Marine Geology*, 192(1–3), 7–22.
- Xie, J., He, Y., Chen, Z., Xu, J. and Cai, S., 2015. Simulations of internal solitary wave interactions with mesoscale eddies in the northeastern South China Sea. *Journal of Physical Oceanography*, 45(12), 2959–2978.
- Xie, Z., Sun, L., Pang, X., Zheng, J. and Sun, Z., 2017. Origin of the Dongsha event in the South China Sea. *Marine Geophysical Research*, 38(4), 357–371.
- Xie, X. et al., 2018. Deep Sea Currents Driven by Breaking Internal Tides on the Continental Slope. *Geophysical Research Letters*, 45(12), 6160–6166.
- Yang, Q., Tian, J. and Zhao, W., 2010. Observation of Luzon Strait transport in summer 2007. *Deep Sea Research Part I: Oceanographic Research Papers*, 57(5), 670–676.

- Yang, W., Zheng, H., Xie, X., Zhou, B. and Cheng, X., 2008. East Asian summer monsoon maximum records in northern South China Sea during the early Holocene (in Chinese). *Quaternary Sciences*, 28(3), 425–430.
- Yin, S., Wang, L., Guo, Y. and Zhong, G., 2015. Morphology, sedimentary characteristics, and origin of the Dongsha submarine canyon in the northeastern continental slope of the South China Sea. *Science China Earth Sciences*, 58(6), 971–985.
- Zhang, W., Cui, Y., Santos, A.I. and Hanebuth, T.J., 2016a. Storm - driven bottom sediment transport on a high - energy narrow shelf (NW Iberia) and development of mud depocenters. *Journal of Geophysical Research: Oceans*, 121(8), 5751–5772.
- Zhang, W., Hanebuth, T.J.J. and Stöber, U., 2016b. Short-term sediment dynamics on a meso-scale contourite drift (off NW Iberia): Impacts of multi-scale oceanographic processes deduced from the analysis of mooring data and numerical modelling. *Marine Geology*, 378, 81–100.
- Zhang, W., Didenkulova, I., Kurkina, O., Cui, Y., Haberkern, J., Aepfler, R., Santos, A.I., Zhang, H., & Hanebuth, T.J.J., 2019. Internal solitary waves control offshore extension of mud depocenters on the NW Iberian shelf. *Marine Geology*, 409, 15-30.
- Zhang, Z., Fringer, O. and Ramp, S., 2011. Three - dimensional, nonhydrostatic

- numerical simulation of nonlinear internal wave generation and propagation in the South China Sea. *Journal of Geophysical Research: Oceans*, 116(C5).
- Zhang, Z., Zhao, W., Qiu, B. and Tian, J., 2017. Anticyclonic eddy sheddings from Kuroshio loop and the accompanying cyclonic eddy in the northeastern South China Sea. *Journal of Physical Oceanography*, 47(6), 1243–1259.
- Zhang, Z., Zhao, W., Tian, J. and Liang, X., 2013. A mesoscale eddy pair southwest of Taiwan and its influence on deep circulation. *Journal of Geophysical Research: Oceans*, 118(12), 6479–6494.
- Zhang, Z., Zhao, W., Tian, J., Yang, Q. and Qu, T., 2015. Spatial structure and temporal variability of the zonal flow in the Luzon Strait. *Journal of Geophysical Research: Oceans*, 120(2), 759–776.
- Zhao, S., Wu, S., Shi, H., Dong, D., Chen, D., Wang, Y., 2012. Structures and dynamic mechanism related to the Dongsha movement at the northern margin of South China Sea. *Progress in Geophysics*, 27, 1008–1019 (In Chinese).
- Zhao, W. et al., 2014. Deep water circulation in the Luzon Strait. *Journal of Geophysical Research: Oceans*, 119(2), 790–804.
- Zhao, Y. et al., 2015. In situ observation of contour currents in the northern South China Sea: Applications for deepwater sediment transport. *Earth*

and Planetary Science Letters, 430, 477–485.

Zheng, X. et al., 2016. Deepwater circulation variation in the South China Sea since the Last Glacial Maximum. *Geophysical Research Letters*, 43(16), 8590–8599.

Zhou, C., Zhao, W., Tian, J., Yang, Q. and Qu, T., 2014. Variability of the deep–water overflow in the Luzon Strait. *Journal of Physical Oceanography*, 44(11), 2972–2986.

### Figure captions

**Fig. 1** Regional bathymetric map of the northern South China Sea, including its regional ocean circulation pattern. Light blue, pink, and white lines mark surface, intermediate, and deep to bottom water circulation, respectively. The white dotted line running north-south represents the location of oceanographic observations in Fig. 2. The red box marks the location of the study area indicated in Fig. 3. SW = surface water; IW = intermediate water circulation; DW = deep water circulation; BW = bottom water circulation.

**Fig. 2** Vertical water column sketch indicating the flow velocity (cm/s) across the Luzon Strait in the east of this study area (adapted from Tian et al., 2006). Positive velocity values denote eastward flow while negative values denote westward flow. The area experiencing westward flow is

shaded in grey. Abbreviations for water masses in Fig. 1. The blue line marks the zero contours. UBW = upper core of BW; LBW = lower core of BW. Fig. 1 shows profile location.

**Fig. 3** A) Multibeam bathymetric map of the study area. B) Regional morphosedimentary map of the study area including the main contourite depositional, erosional, and mixed features. Surface traces of the seismic reflection profiles and those interpreted in this study are shown by respective thin and thick white lines in A). Associated figure numbers are shown along the seismic lines in A). Black circles indicate sediment cores and wells and grey points indicate current velocity observations. CS = canyon system; CC = contourite channel; E = elevation or elevated feature.

**Fig. 4** Seismic reflection profiles showing contourite drifts and associated channels. A) Seismic profile across Drift-1; B) enlarged image of CC-1; C) seismic profile across Drift-2 and two piston cores from this drift (SC1 adapted from Yang et al., 2008; SC2 adapted from Huang et al., 2015). Black lines mark regional seismic discontinuities (H5 to H1) and thick black lines denote positions of cores and wells. SU = Seismic unit; WB = Wavy bedforms; TWT = two-way travel time. See Fig. 3A for the location of the seismic profiles.

**Fig. 5** Seismic reflection profiles show contourite Drift-3 (A, B) and Drift-4 (C)

as well as contourite channels (CC-2), moats, and sub-circular / oval depressions. Black lines mark regional seismic discontinuities (H5 to H1).

SU = Seismic unit; WB = Wavy bedforms; TWT = two-way travel time.

See Fig. 3A for seismic profiles locations.

**Fig. 6** Seismic profile (A) constrained by ODP site 1144 well data and including synthetic seismograms (B) and age data (C) corresponding to benthic  $\delta^{18}\text{O}$  records (Lisiecki and Raymo, 2005). D) Photos of core material from different depths (C1, C2, C3; locations given in B). The sedimentary log is modified from Wang et al. (2000). Age-depth model from Bühring et al. (2004). Numbers in C) denote marine isotope stages (MIS) during glacial stages.

**Fig. 7** Hill shade map (A) and seismic reflection profile (B) showing wavy bedforms as well as moats and irregular sub-circular / oval depressions on Drift-2. Wavy bedforms migrate upslope or downslope and show asymmetric cross sections. C) Seismic reflection profile showing the middle slope contourite terrace. Fig. 3A shows seismic profile location.

**Fig. 8** Diameter (A) and depth (B) of irregular sub-circular / oval depressions in the study area with dashed lines marking 2000 m water depth. Wavelength (C), wave height (D), and orientation (E) of wavy bedforms. The dashed and dotted boxes in (E) indicate respective tangent trends of modern internal waves and their reflections in the northern South China Sea (from

Zhang et al., 2011).

**Fig. 9** Hill shade map (A) and 3-D bathymetric-seismic images (B and C) showing irregular sub-circular / oval depressions on Drift-3 and Drift-4 in the study area. These depressions are situated around elevated features E1, E2, and E5. Blue lines in (A) mark the surface trace of seismic profiles in (B) and (C). Red crosses denote eleven points (P1 to P11) used to model flow speeds around five depressions as shown in (A).

**Fig. 10** Numerical simulation of the bottom stress on the seafloor and flow velocity in the study area for two scenarios. Scenario 1 represents anticyclonic mesoscale eddy propagation, while Scenario 2 represents cyclonic mesoscale eddy propagation. Note the formation of many sub-mesoscale eddy currents around bathymetric highs. Locations overlap with those of the irregular depressions exhibiting analogous dimensions and shape. Red lines outline the main irregular depressions described in this study.

**Fig. 11** Flow speed estimates inside and outside of five local sub-circular / oval depressions during a mesoscale anticyclonic (Scenario 1) and cyclonic (Scenario 2) eddy cycle (45 days) from numerical simulation. A to E show flow speed estimates from five local depressions during an anticyclone eddy cycle while F to J show flow speed estimates for the same position during a cyclonic eddy cycle. The left axes denote duration of the flow

speed over a 45 day eddy cycle. The white box with black boundaries marks points within depressions while black and grey boxes represent points outside depressions. In general, higher flow speeds occur within depressions over longer intervals relative to those outside depressions. See point (P1–P11) locations in Fig. 9A.

**Fig. 12** Simulated near-bottom suspended sediment (ml/l) concentrations during a bottom-generated cyclonic eddy (Scenario 2). Mesoscale eddies transport clays and induce deposition close to topographic highs. Depth contours are plotted in grey with an interval of 50 m between 1500 and 4500 m water depth. Blue circles show center positions for eddies in each situation.

**Fig. 13** Seismic and vertical hydrographic sections south (A) and southeast (B) of the Dongsha Islands. Profile locations shown in Fig. 3A.

**Fig. 14** Hydrographic measurements of bottom current velocities for M1 (A), M2 (B), and M3 (C) sites on Drift-2 (modified from Zhao et al., 2015; Zhang et al., 2013, and Dong et al., 2015). A) and B) show that intermittent mesoscale eddies could significantly increase the flow velocity of regional water masses in this study area; C) shows that periodic internal waves could also enhance flow velocity. Site locations shown in Fig. 3A.

**Fig. 15** 3D Sketch of the northern South China Sea including primary and

secondary contourite features and their association with long- and short-term oceanographic processes. Regional circulation of water masses determines the position of contourite depositional (drifts and sedimentary waves), erosional (channels, moats and furrows), and mixed (terraces and irregular depressions) features at different water depths (see text for further discussion). CS1 to CS7 illustrate the position of major submarine canyons systems. Features E1 to E10 represent prominent bathymetric highs and CC-1 and CC-2 indicate positions of larger contourite channels. Yellow areas show smaller contourite channels, moats, and furrows. Smaller furrows along the slope are shown in black. CDS = contourite depositional systems. Legend for contourite drift: PD = Sheeted plastered drifts; SD = Mounded elongated and separated drifts. Legend for water masses: IW = Intermediate water mass; DW = Deep Water mass; BW = Bottom water mass. IWs = Internal waves.

**Highlights**

- Multidisciplinary approach is used to investigate oceanographic process interaction for contourite development;
- There is a hierarchy of features associated to different scale oceanographic processes;
- Regional water mass circulations are responsible for primary large-scale contourite features;
- Mesoscale eddies generate medium- and small-scale depressions superposed on the large-scale features;
- Internal waves form sediment waves as secondary depositional features on the large-scale drifts.

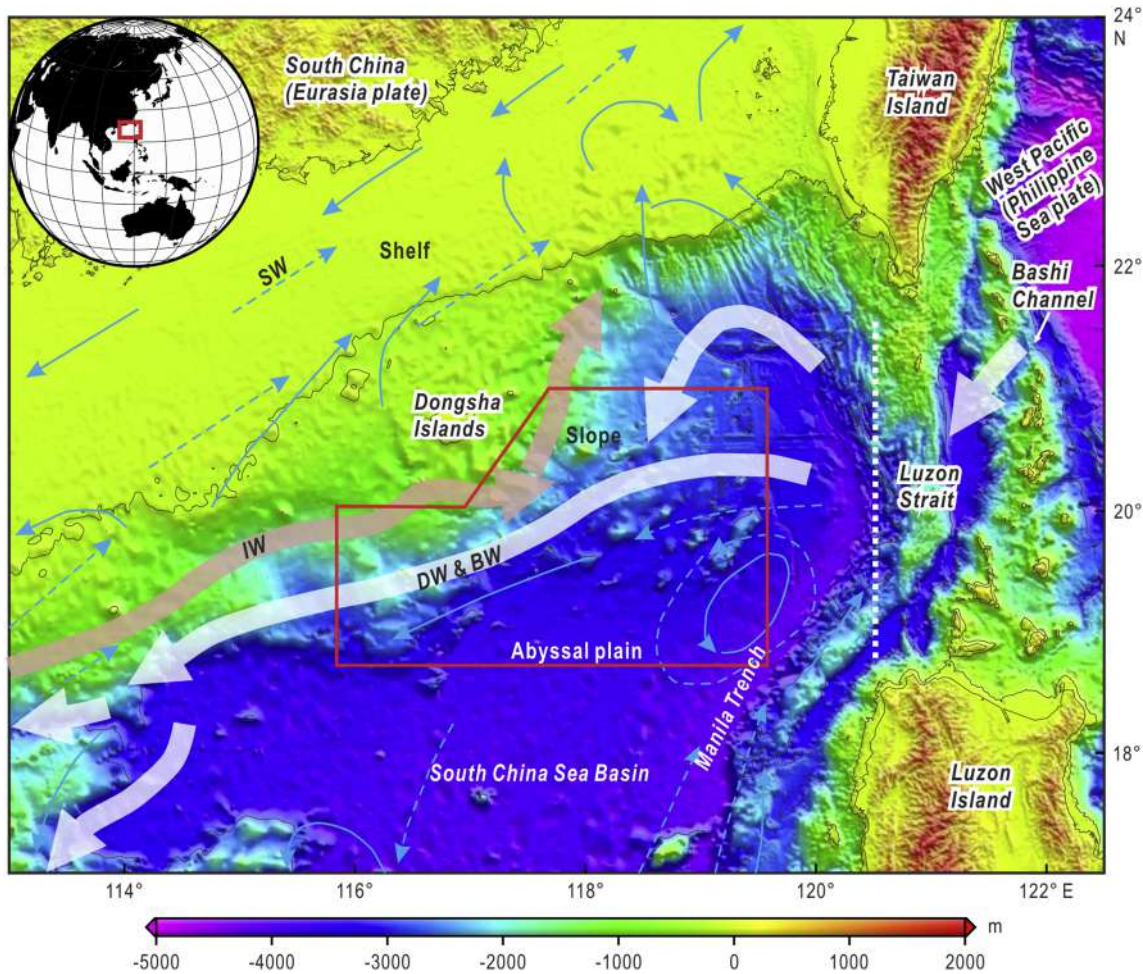


Figure 1

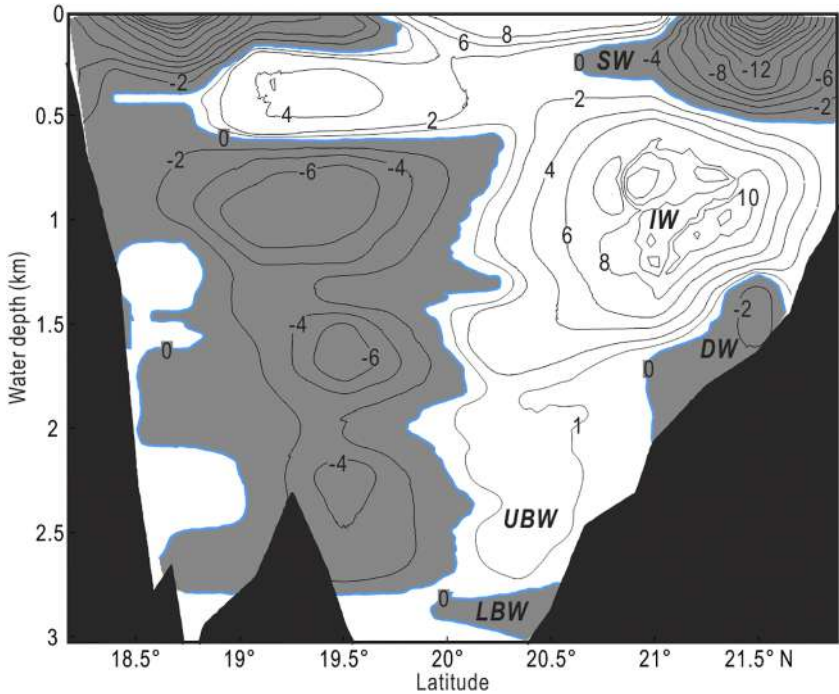


Figure 2

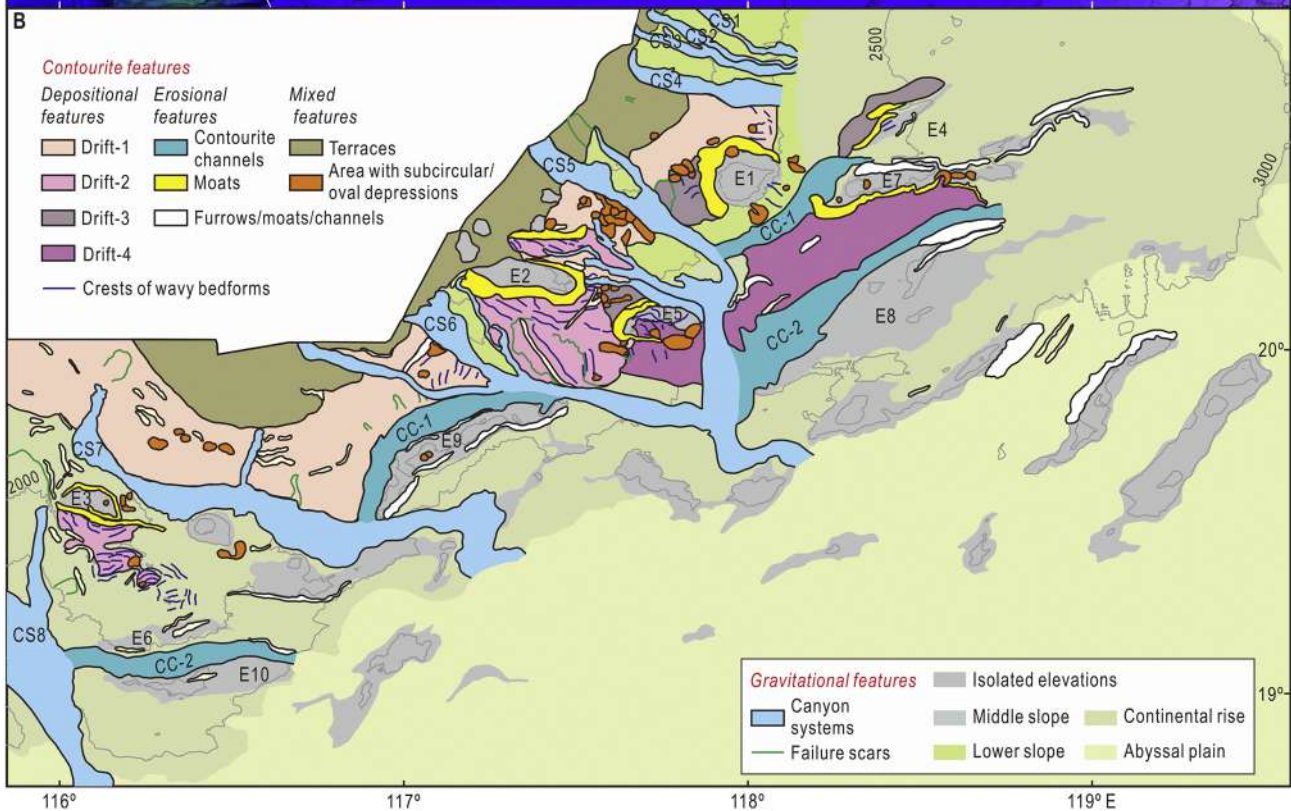
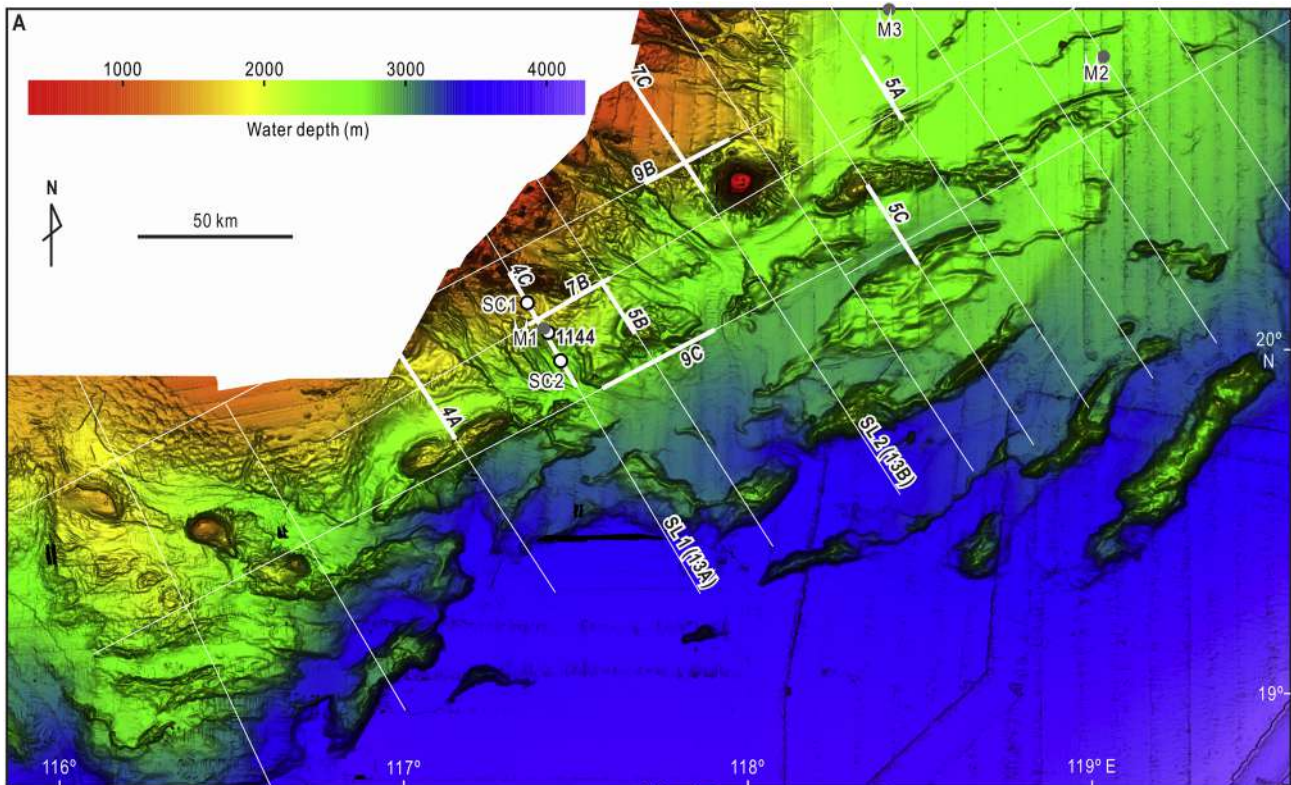


Figure 3

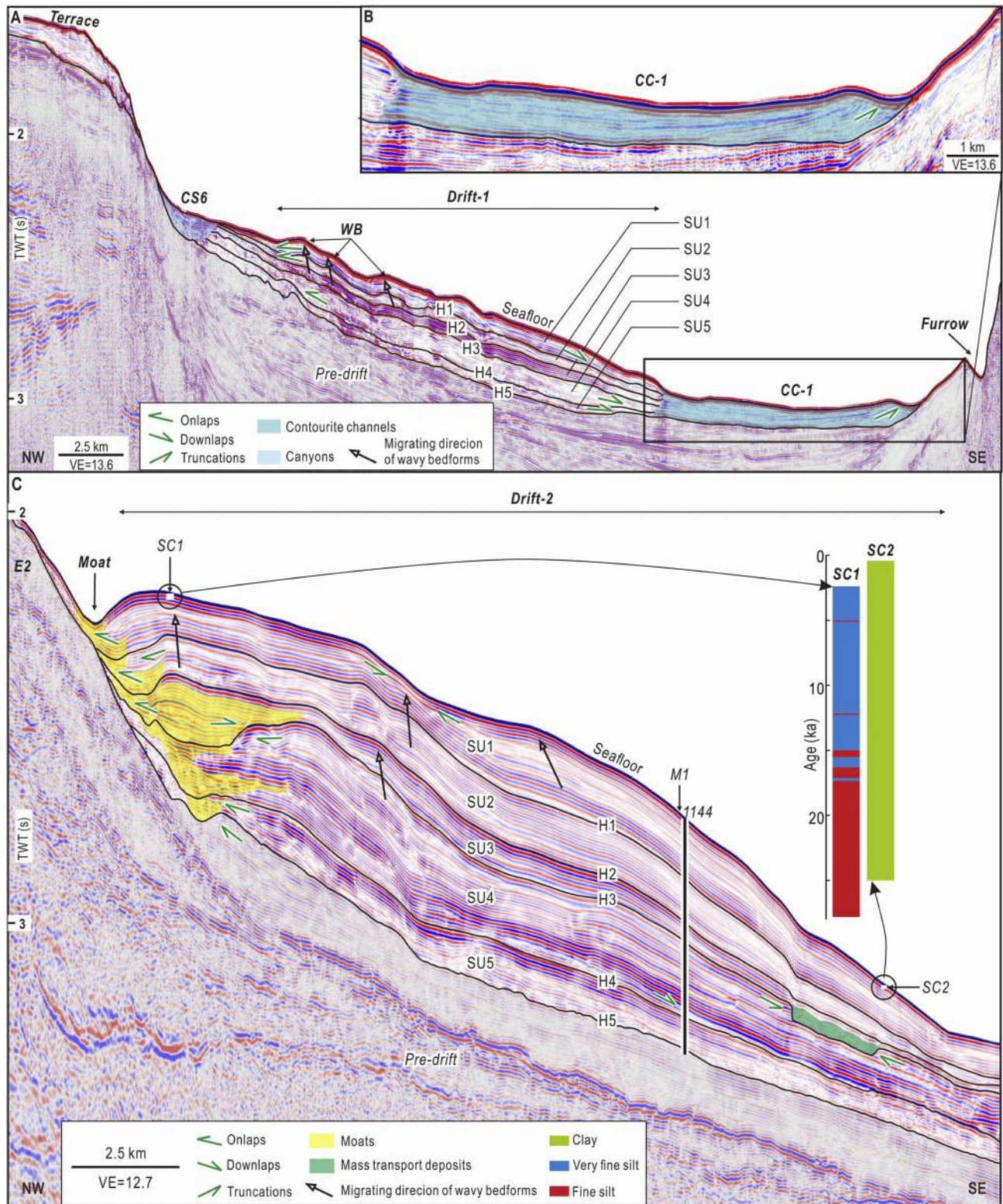


Figure 4

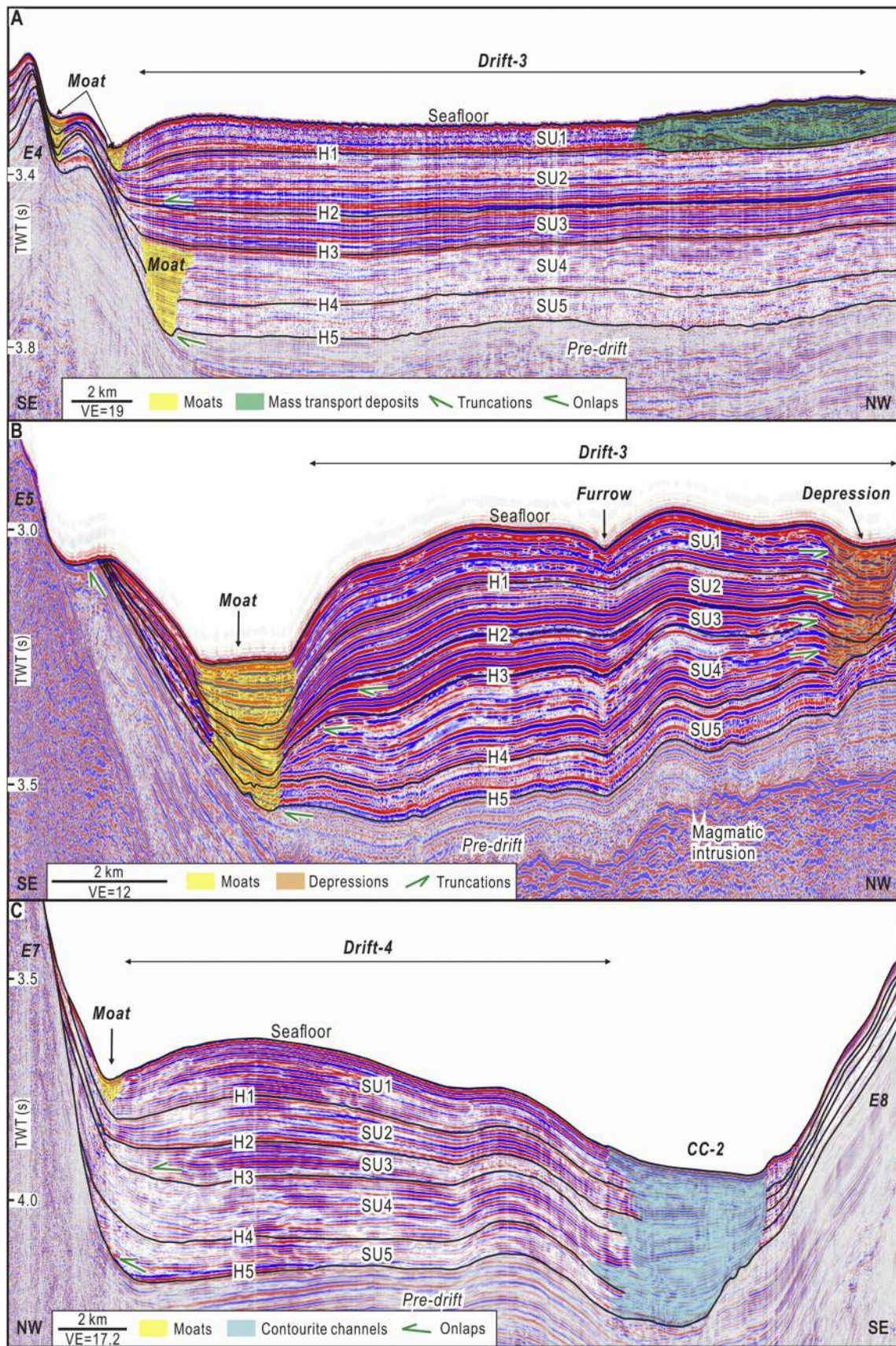


Figure 5

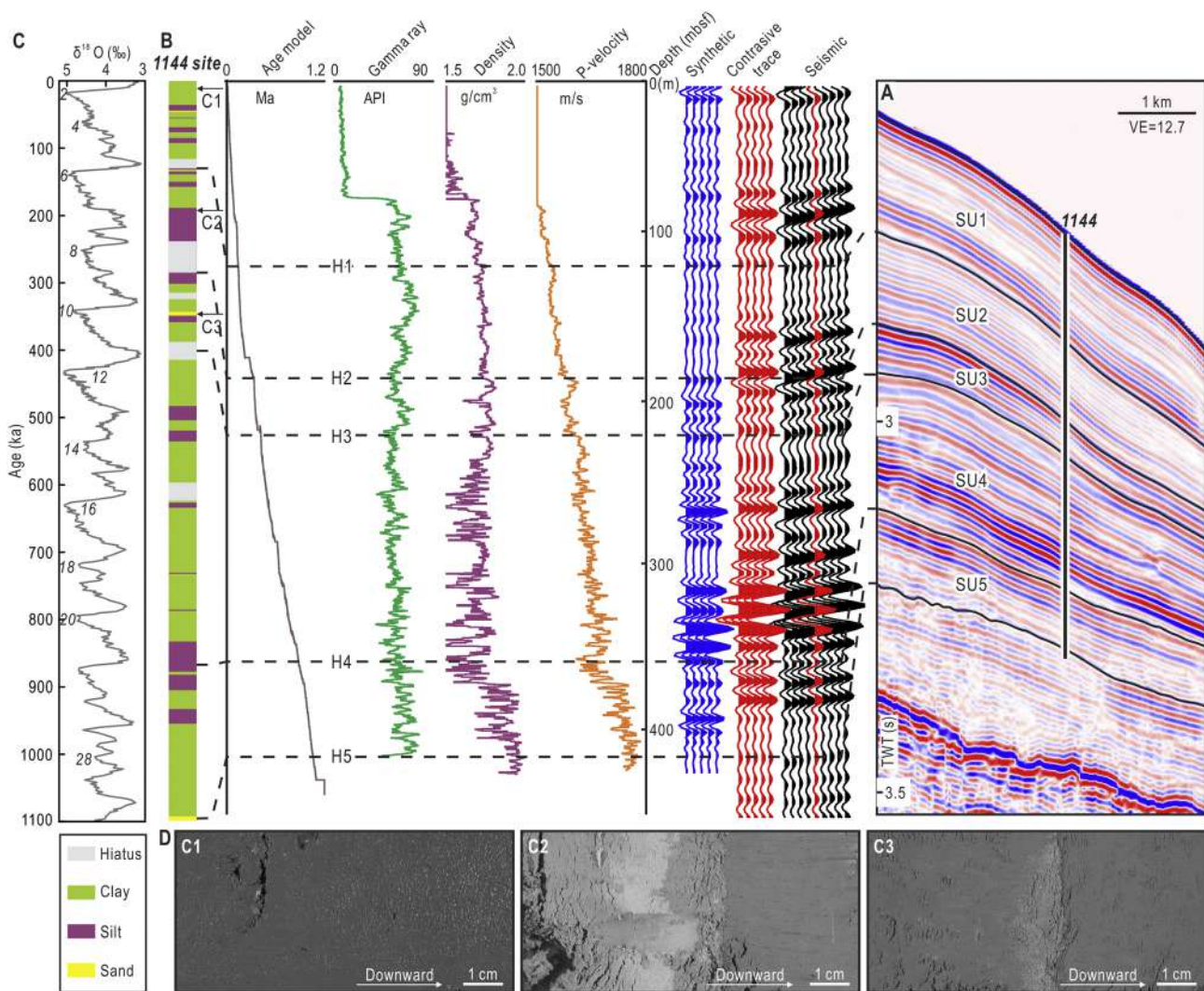


Figure 6

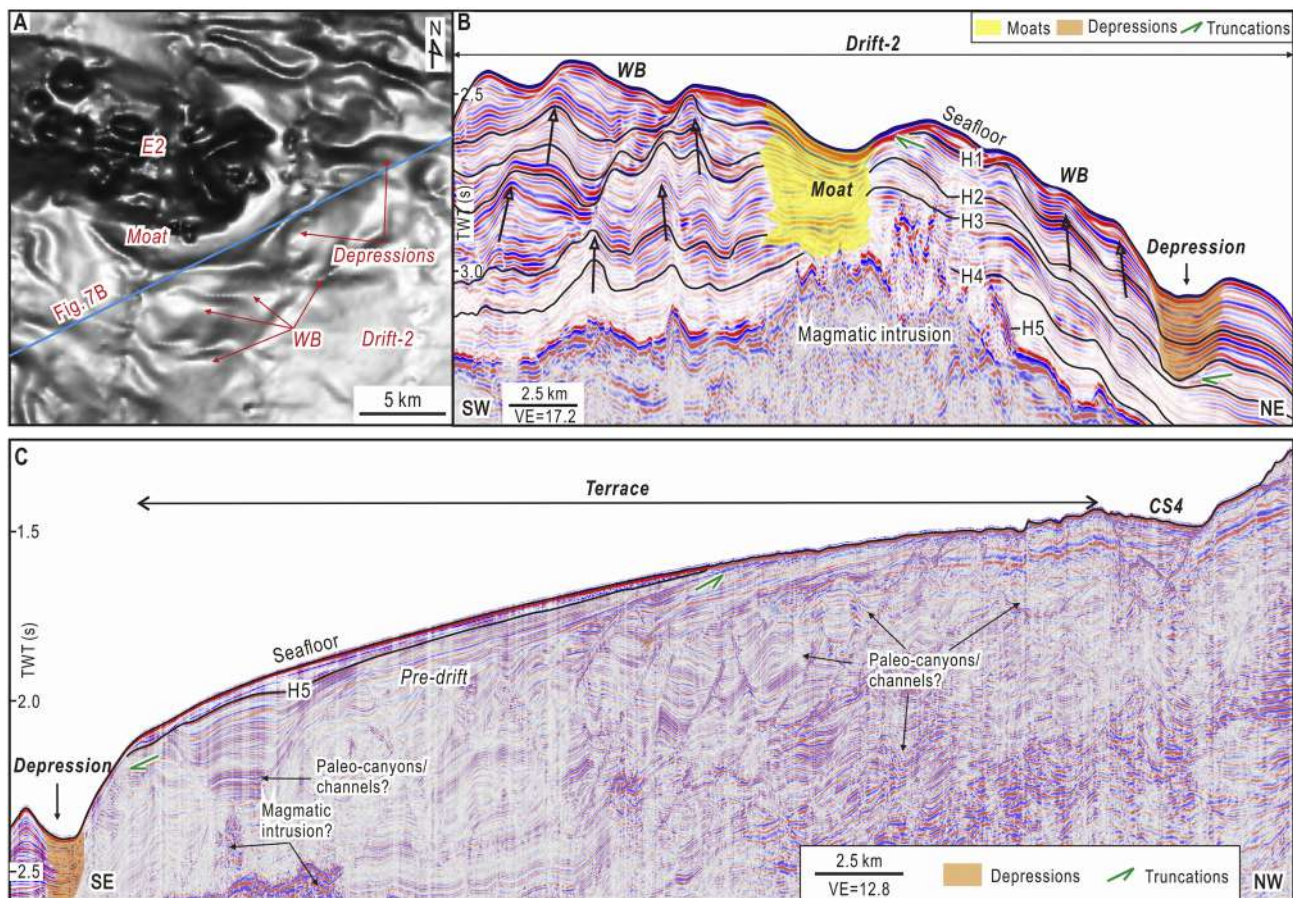


Figure 7

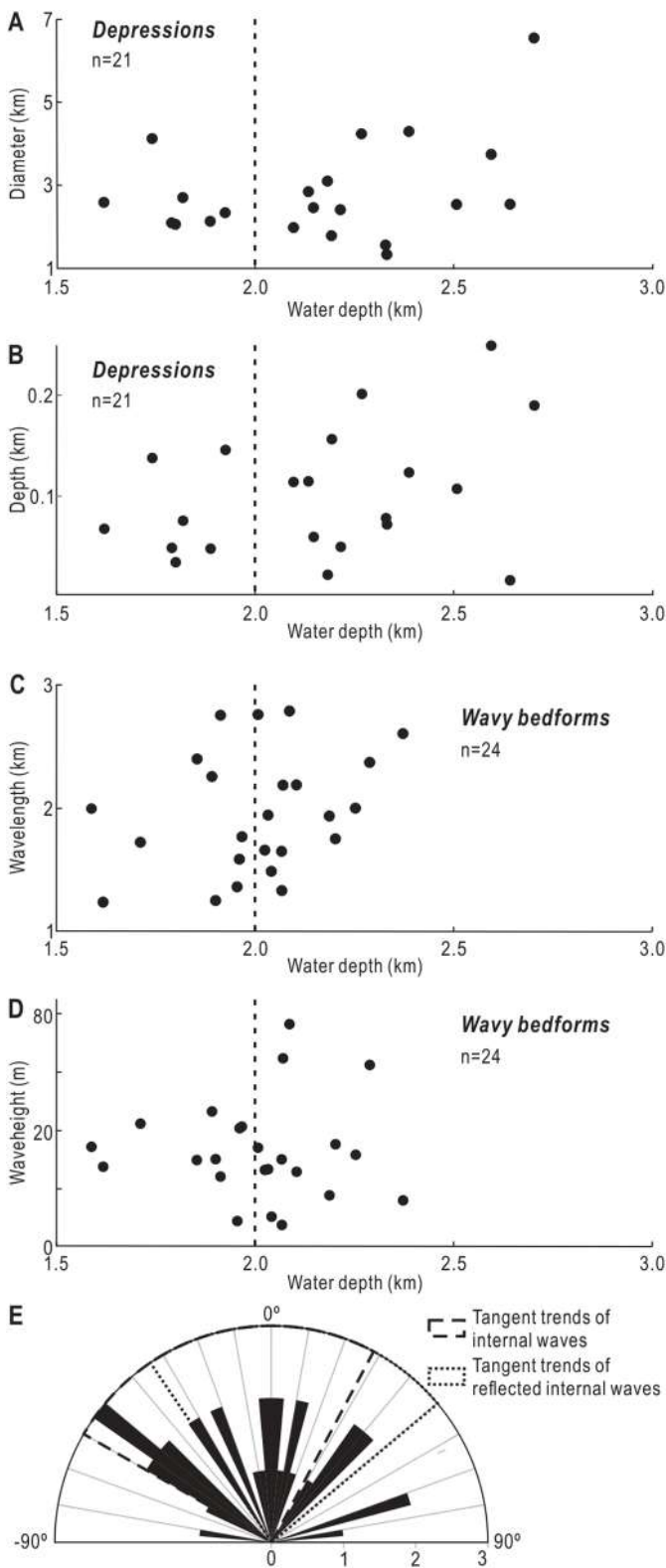


Figure 8

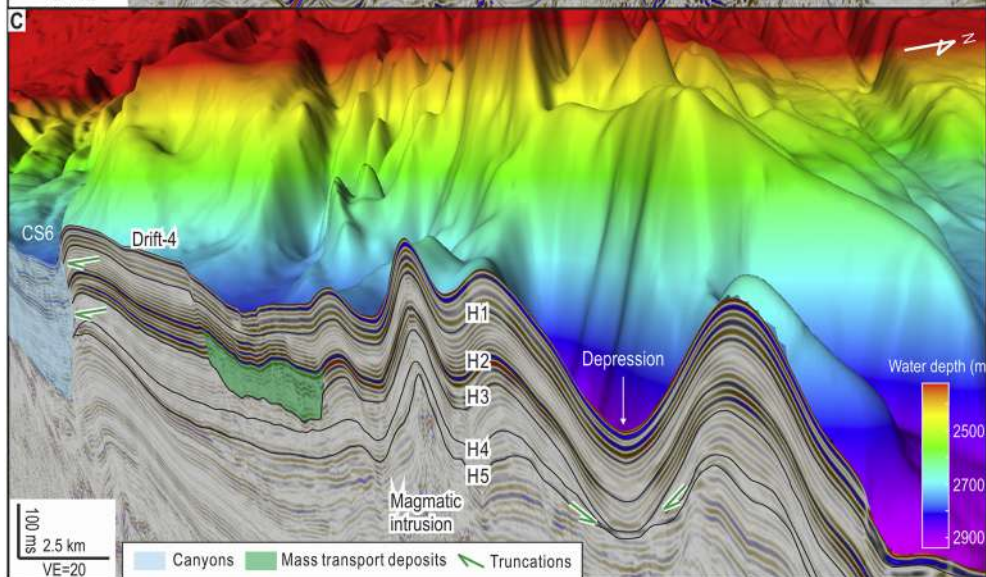
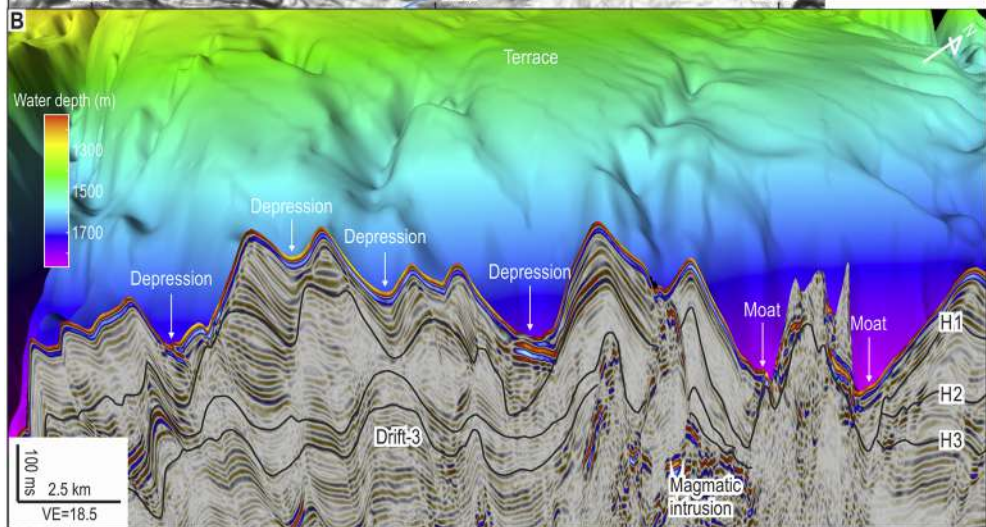
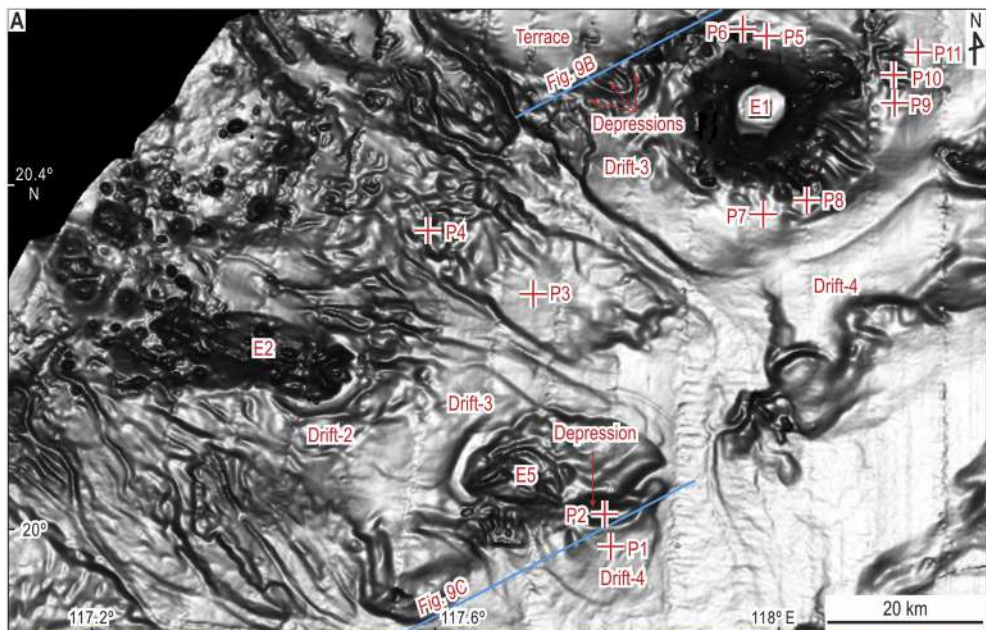


Figure 9

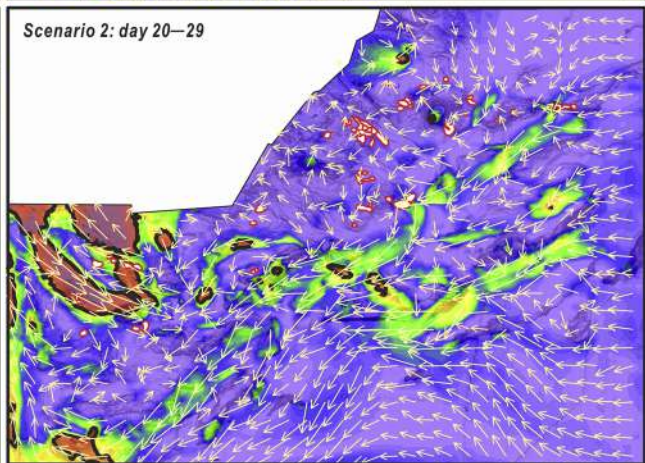
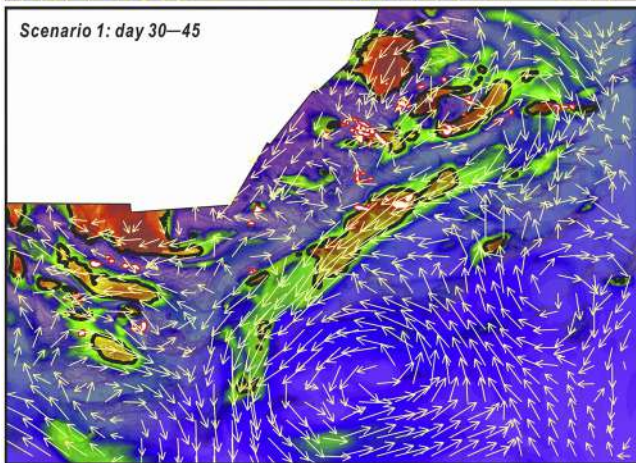
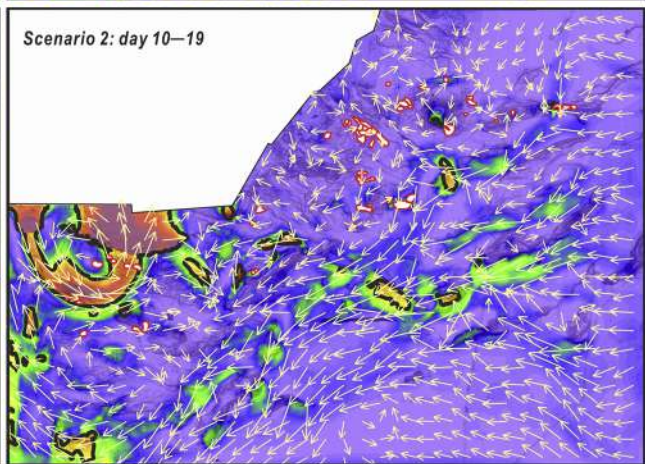
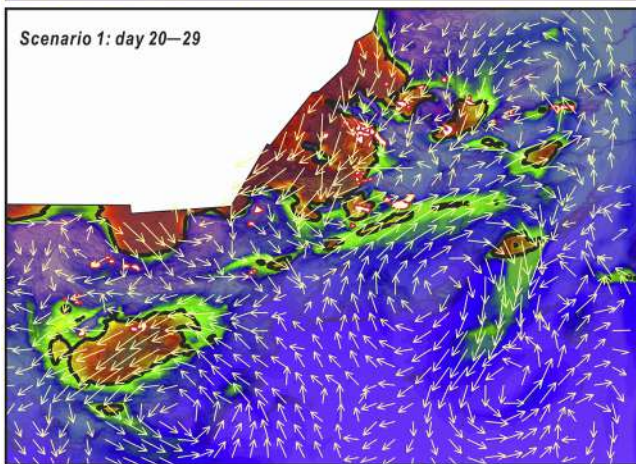
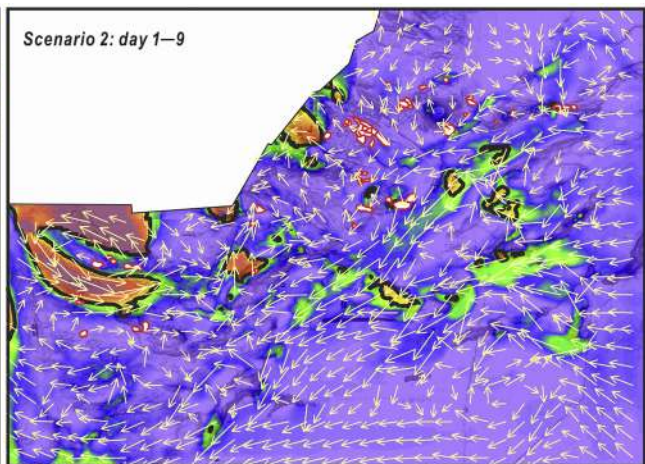
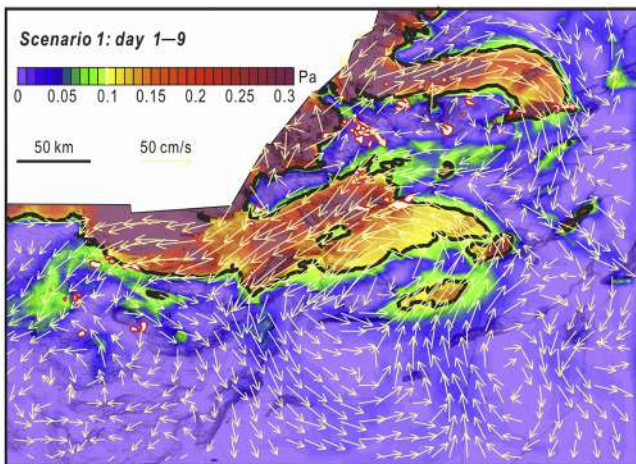


Figure 10

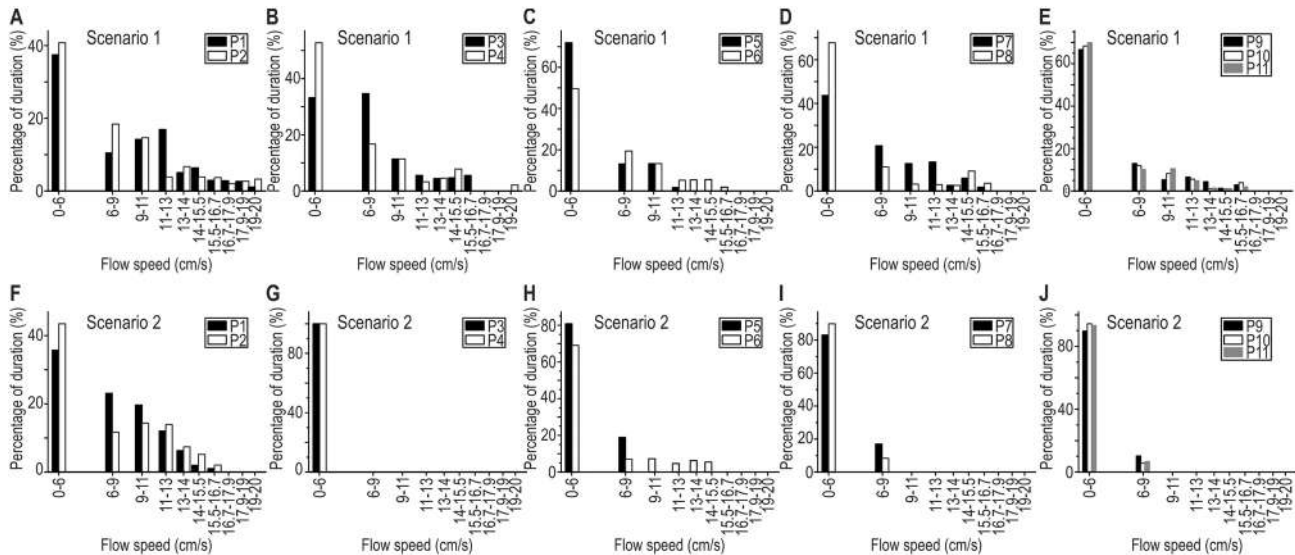


Figure 11

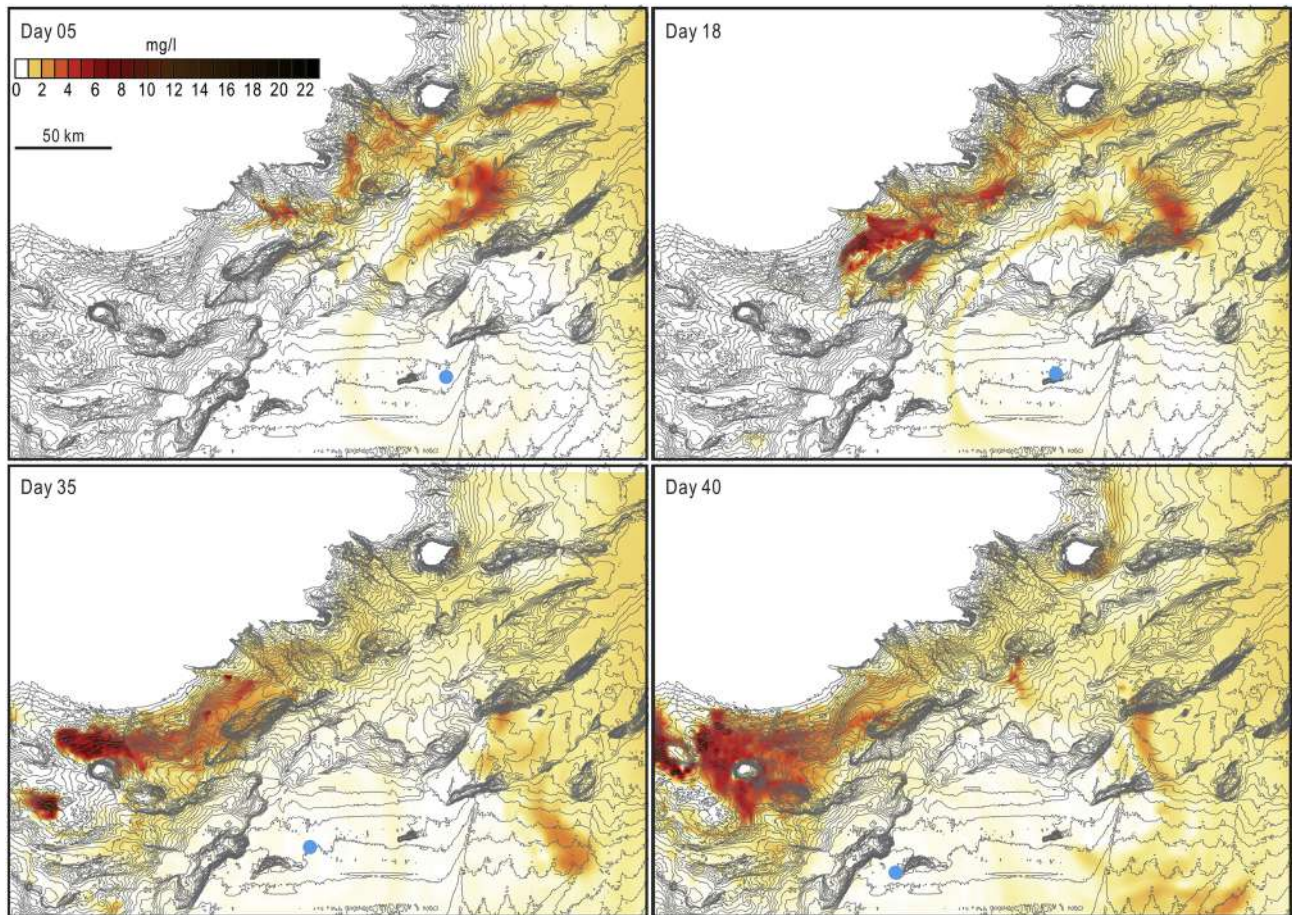


Figure 12

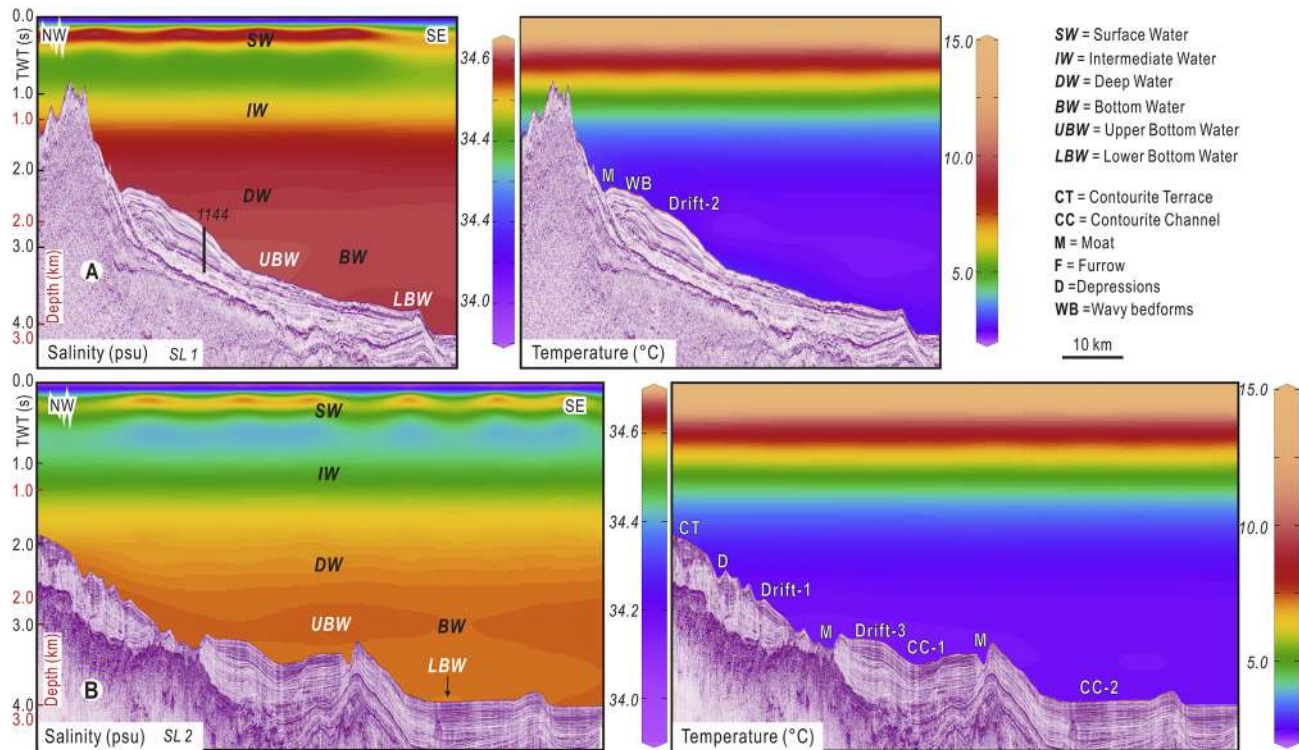


Figure 13

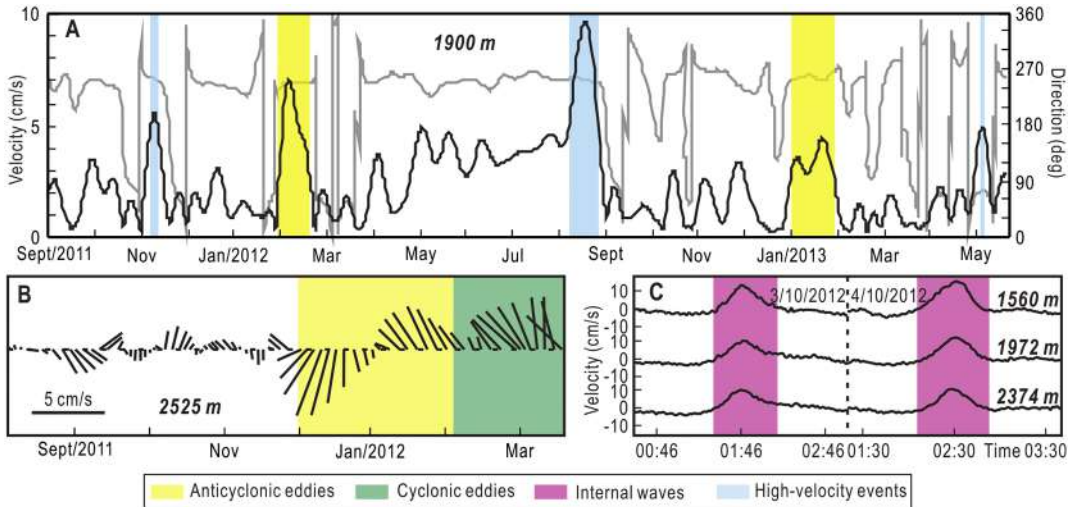


Figure 14

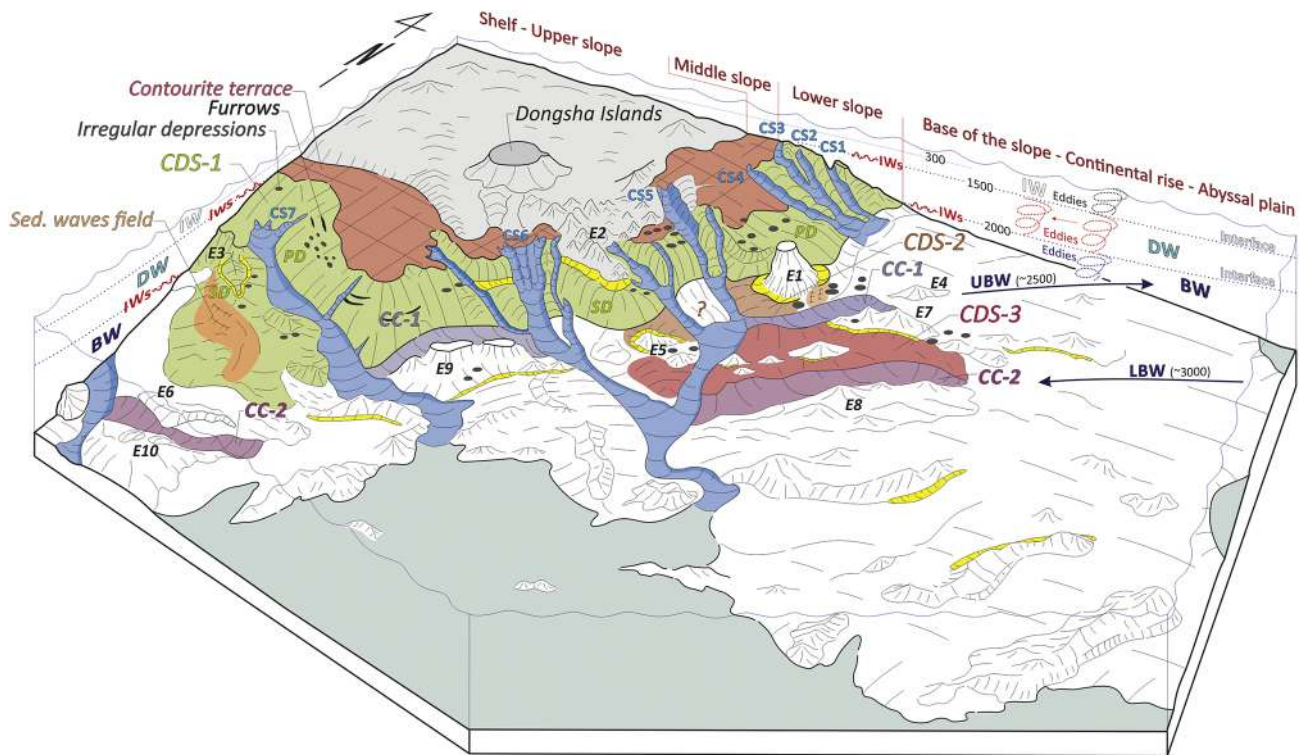


Figure 15